X-Band Radar and Surface-Based Observations of Cold-Season Precipitation in Western Colorado's Complex Terrain

STELLA HEFLIN,[a] MIMI ABEL,[b] SOUNAK BISWAS,[b,c] ANNARELI MORALES,[d] ROB CIFELLI,[b] JOSEPH SEDLAR,[e,f]
DANIEL FELDMAN,[g] V. CHANDRASEKAR,[c] AND PATRICK KENNEDY[c]

[a] *Department of Atmospheric Sciences, University of Washington, Seattle, Washington*
[b] *NOAA/Physical Sciences Laboratory, Boulder, Colorado*
[c] *Department of Electrical and Computer Engineering, Colorado State University, Fort Collins, Colorado*
[d] *Weld County Department of Public Health and Environment, Greeley, Colorado*
[e] *Cooperative Institute for Research in Environmental Sciences, University of Colorado Boulder, Boulder, Colorado*
[f] *NOAA/Global Monitoring Laboratory, Boulder, Colorado*
[g] *Lawrence Berkeley National Laboratory, Berkeley, California*

(Manuscript received 1 September 2023, in final form 16 June 2024, accepted 23 July 2024)

ABSTRACT: Hydrologic processes associated with intermountain cold-season precipitation in the Upper Colorado River basin have important impacts on avalanche forecasting and water resource management. However, traditional weather radar networks struggle with observations in this complex terrain. Data collected during the Study of Precipitation, the Lower Atmosphere, and the Surface for Hydrometeorology (SPLASH) and its sister campaign, Surface Atmosphere Integrated Field Laboratory (SAIL) in the East River watershed of western Colorado, are used to examine a multistorm period from 23 December 2021 to 1 January 2022 that contributed 35% of the total winter precipitation in this watershed. Dual-polarization X-band radar and disdrometer measurements show ~30-mm differences in precipitation amount at two sites in proximity over four distinct storm events within the period. Wind patterns, synoptic forcings, microphysical characteristics of precipitation, and surface meteorology are analyzed to explain the observed spatial variability of cold-season precipitation in complex mountainous terrain. Analysis shows that differences over time within this event are mainly accounted for by synoptic forcings, such as frontal passages; differences between sites are accounted for by the impact of variations in local wind patterns on precipitation microphysics. Patterns of surface precipitation intensity are compared and found to be correlated with X-band radar signatures; a relationship between a strong dendritic growth stage and intense low-density surface precipitation is reinforced by this study. This relationship demonstrates the importance of particle growth mechanisms on surface snowfall patterns in high-altitude complex terrain, underscoring the importance of realistic microphysical parameterizations.

SIGNIFICANCE STATEMENT: The amount and density of snowpack from western Colorado winter storms have significant impacts on water resources in the Upper Colorado River basin. Snowpack characteristics are affected by small-scale differences in how snow forms in the atmosphere. These differences are hard to study in the complex terrain of the Rockies, but data from the SPLASH and SAIL field campaigns allows us to investigate how snow crystal formation and mountain-driven wind patterns affect snow near the surface. Our study finds that snow crystal growth varies over small space and time scales and is likely controlled by the terrain beneath a given location and resultant local wind patterns. These results imply that predicting snowpack in the Rockies requires properly representing local wind patterns and crystal growth processes in models.

KEYWORDS: Wind shear; Precipitation; Snowfall; Cloud microphysics; Orographic effects; Radars/Radar observations

1. Introduction

The Colorado River basin supplies water for approximately 40 million people across seven states in the western United States, and its total contribution to basin state economies is one-twelfth of the total U.S. gross domestic product (James et al. 2014; Bureau of Reclamation 2024). Prolonged drought and increasing demand for water resources have led to water shortages in the Colorado River basin, and the situation is expected to worsen as our climate continues to warm (Lukas and Payton 2020). An accurate understanding of the precipitation that falls in the Colorado River watershed is therefore essential to water resource management in the western United States. Due to both topography and large-scale weather patterns, runoff in the Colorado River basin primarily comes from highly productive and mainly snow-fed headwaters in the Upper Colorado River basin (UCRB) of western Colorado (Lukas and Harding 2020). Snow typically accumulates in this watershed during the cold season from October through May, melting during the spring (Lukas and Harding 2020).

Cold-season precipitation events are the dominant contributor to basin streamflow and are a critical input for local avalanche forecasting (Rasmussen et al. 2011; Lukas and Harding 2020;

Supplemental information related to this paper is available at the Journals Online website: https://doi.org/10.1175/JHM-D-23-0147.s1.

Corresponding author: Stella Heflin, smheflin@uw.edu

DOI: 10.1175/JHM-D-23-0147.1

Campbell and Steenburgh 2014; Wasserstein and Steenburgh 2024; Alcott and Steenburgh 2010). However, in areas with complex terrain, winter storms are governed by a variety of complex dynamics and thermodynamics (Smith 1979; Roe 2005; Houze 2012). Factors such as interactions between large-scale flow and boundary layer turbulence, local wind patterns and updrafts, and orographic precipitation enhancement can create significant variability in precipitation totals and characteristics over small spatial scales, on the order of a few kilometers (Ikeda et al. 2010; Geerts et al. 2011; Campbell and Steenburgh 2014; Mott et al. 2018; Houze 2012).

These small spatial scales pose a challenge for the scales of climate and longer-range numerical weather prediction models, which do not currently well-represent complex topography and therefore struggle to accurately predict local-scale winter season precipitation (Ikeda et al. 2010; Campbell and Steenburgh 2014; Rasmussen et al. 2011). Convection-permitting models perform better but still may underestimate snowfall in complex terrain (Ikeda et al. 2010, 2021; Liu et al. 2017; Rasmussen et al. 2023), although their evaluation is fraught by uncertainty in the observations themselves (Bytheway et al. 2024; Lundquist et al. 2019). Furthermore, convective-permitting models' snowpack prediction is sensitive to microphysics parameterization schemes (Xu et al. 2023; Rudisill et al. 2024), i.e., the parameterization of processes that govern the microphysics of ice crystal growth, especially during heavy snowfall events. A lack of observational constraints compounds uncertainty in the interpretation of microphysical relationships (Schrom et al. 2015; Allabakash et al. 2019; Eidhammer et al. 2017). Further exacerbating this challenge, while radar is typically used for the monitoring of current atmospheric conditions and short-term forecasting, the National Weather Service (NWS) Weather Surveillance Radar-1988 Doppler (WSR-88D) network provides poor coverage over much of the western United States due to complex terrain, especially during stratiform winter precipitation events that occur in flat cloud banks between 1 and 3 km above ground level (Bytheway et al. 2024; Maddox et al. 2002). Climatological relationships such as the correlation between altitude and snowpack amount can sometimes be used to help fill knowledge gaps but do not always hold, especially during the thermodynamically driven stages of orographic storms, where updrafts may play a role in forcing snow formation (Ikeda et al. 2010; Campbell and Steenburgh 2014).

Motivated by the need to observationally understand systems that govern snowpack in complex intermountain terrain, NOAA's Study of Precipitation, the Lower Atmosphere, and the Surface for Hydrometeorology (SPLASH) field campaign and DOE ARM's collocated Surface Atmosphere Integrated Field Laboratory (SAIL) campaigns were launched (de Boer et al. 2023; Feldman et al. 2021; Feldman et al. 2023). Both campaigns have a comprehensive instrument network in the East River watershed (ERW) near Crested Butte, Colorado (Fig. 1). This network includes a SPLASH X-band radar with a clear view of the southeast–-northwest oriented East River Valley, a SAIL X-band radar that looks north from the north face of Mount Crested Butte, as well as field sites along the valley with Particle, Size, and Velocity (PARSIVEL) disdrometers and meteorological observing stations.

The combination of SPLASH and SAIL's dual-polarization (hereafter, dual-pol) X-band radar datasets provides a unique ability to look in detail at the microphysical and kinematic characteristics of a significant precipitation event in complex terrain. Several studies have noted relationships between specific radar-observed dual-pol variables, including horizontal reflectivity (Z_H), differential reflectivity (Z_{DR}), specific differential phase (K_{DP}), and cross-polarized correlation coefficient (ρ_{HV}), and particle growth mechanisms (i.e., accretion, deposition, and aggregation) that determine the type, size, and density of ice crystals (Bringi and Chandrasekar 2001; DeVoir 2002; Bechini and Chandrasekar 2015; Kumjian 2013b; Kumjian et al. 2014; Schneebeli et al. 2013; Bechini et al. 2013). These relationships between radar observations, particle growth mechanisms, and subsequent particle types can be further analyzed through the use of precipitation typing algorithms; one example is the Bechini and Chandrasekar (2015) classification system used in this analysis.

This paper focuses on the relationships between the observed microphysical characteristics of ice crystals in the atmosphere and near-surface snowfall amounts, with implications for the density of the resulting snowpack. The implications arise primarily because the particle types and growth processes, indicated by dual-pol radar signatures, result in different particle densities at the surface. For instance, previous studies have found that aggregate particles tend to be relatively less dense than rimed particles (Ishizaka et al. 2016; Brandes et al. 2007). In fact, within events that are warmer and dominated by aggregates, an increase in particle diameter is associated with a decrease in bulk density of both hydrometeors and fresh snowfall (Judson and Doesken 2000; Brandes et al. 2007; Tiira et al. 2016; Yin and Yuan 2022). As such, snow microphysical characteristics can play a crucial role in accumulations, and there is a close connection between snow particle structure (i.e., hydrometeor type resulting from a specific growth process) and bulk snowfall density (DeVoir 2002; Kneifel and Moisseev 2020; Brandes et al. 2007; Tiira et al. 2016). Furthermore, studies of snow density in the Rocky Mountains have found that new snowfall density is strongly affected by orographic forcings and can vary dramatically over short distances, enhancing the complexity of this analysis (Judson and Doesken 2000). The following investigation builds off previous studies to explore direct connections between snow microphysics—as inferred from radar and disdrometer observations—and snowpack, inferred from near-surface snowfall observations and snow depth observations.

This analysis focuses on a case study event known to residents in Crested Butte, Colorado, as the "Santa Slammer" that occurred over a 10-day period from 23 December 2021 to 1 January 2022 within an anomalously moist atmosphere for this region and time of year (M. Meyers, National Weather Service, 2023, personal communication). The event was not one continuous storm, but rather a series of four distinct storms that occurred in quick succession, each with their own unique characteristics, resulting in significant snow accumulation. Each of the four storms was associated with an interior-penetrating atmospheric river (AR) passage (Rutz et al. 2014; Rutz and Steenburgh 2012; Rutz et al. 2015). This multistorm event was the largest of the season, accounting for 35% of

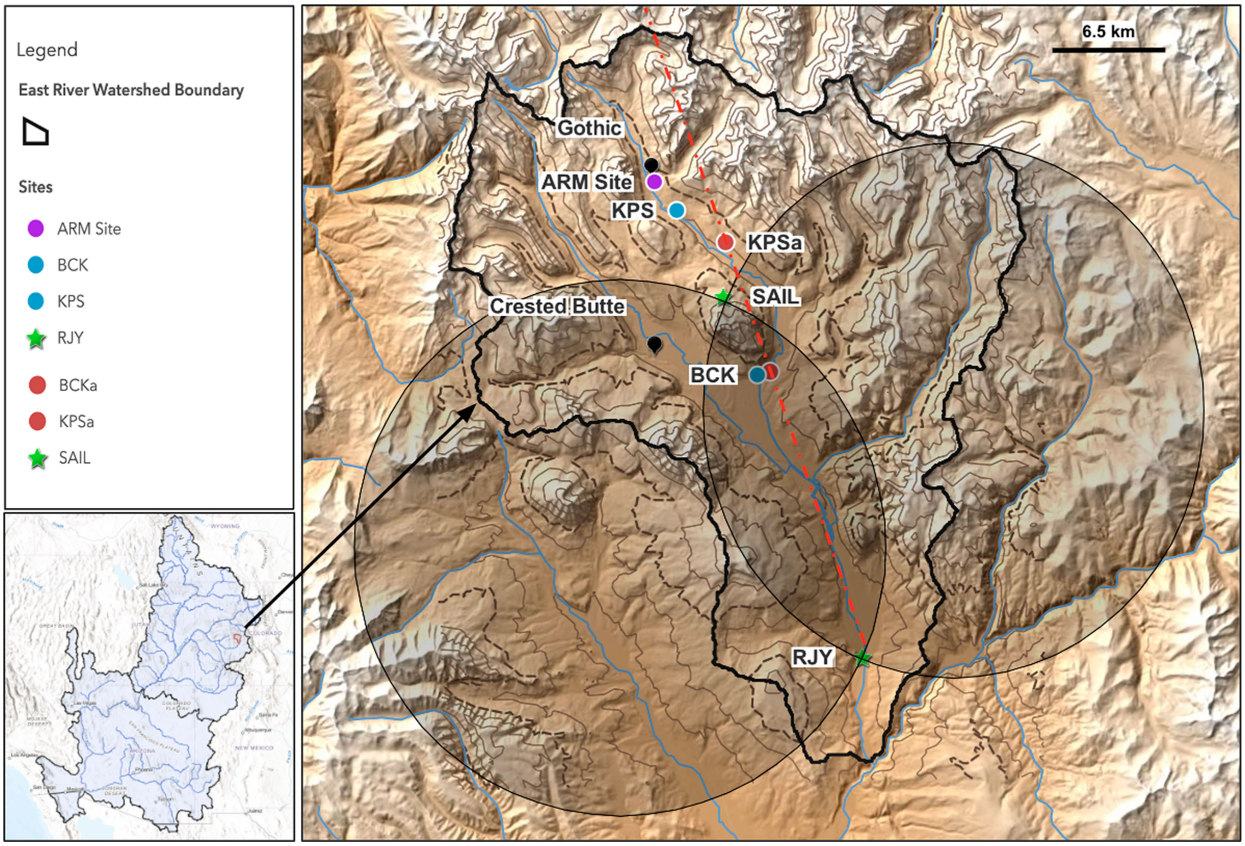

FIG. 1. Map of topography showing the field sites: KPS at 2863 m ASL, BCK at 2723 m ASL, RJY at 2504 m ASL, SAIL at 3137 m ASL, and ARM site (purple circle, radiosonde launch point) at 2891 m ASL. Green stars denote radar sites, and blue circles denote field sites with disdrometers and rain gauges. The alternative sites used for radar data analysis, KPSa and BCKa (red circles), are also included. Relevant geographic reference points (Crested Butte and Gothic) and the ERW boundary (solid black outline) are provided for reference. Lower-left corner shows the ERW's location within the Colorado River basin. The straight dashed red line across the figure represents the 342° azimuth line from RJY that the RHI figures are displayed along. The light circles represent the coverage region of the dual-Doppler analysis; the darker shaded region in the center is along the baseline between the two radars; and therefore, dual-Doppler cannot be calculated in this region. The contour lines are at 200-m intervals, and the thicker dashed contour line represents 3000 m.

total winter season precipitation accumulated at a nearby measurement site on Mount Crested Butte (National Water and Climate Center 2022). The precipitation from this event was largely stratiform within each storm period. Radar echo-top heights were below 6.0 km above mean sea level (MSL), generally less than 2.0 km above the peaks of nearby terrain. The goal of this observational analysis is to explore temporal and spatial differences in precipitation at the surface during a hydrologically crucial set of storms and connect surface snowfall differences to microphysical characteristics of ice particles in the atmosphere.

2. Study region and data

a. Site description

The ERW is located in highly complex terrain deep in the Rocky Mountains of western Colorado within the UCRB (Fig. 1). Crested Butte and Gothic, Colorado, are used as geographic reference points in describing the field sites. The SPLASH X-band radar is located at the Roaring Judy fish hatchery (RJY). The SAIL X-band radar is located on the north slope of Mount Crested Butte, the isolated mountain in the center of the figure. The ARM site to the immediate south of Gothic is the launching point for the twice daily (1130 and 2330 UTC) SAIL radiosondes.

The Kettle Ponds (KPS) site is located in the inner valley of the ERW, approximately 1.6 km southeast from Gothic. The KPS site is ~27 km northwest from the SPLASH radar and roughly 300 m upslope from the East River to the northeast of its banks. The Brush Creek (BCK) site is on the southwest side of Mount Crested Butte, roughly 5 km from Crested Butte, Colorado. The BCK site is ~17 km northwest from the SPLASH radar and roughly 200 m upslope from the East River to the northwest of its banks. KPS and BCK are roughly 10 km apart.

The closest WSR-88D (KGJX) is located near Grand Junction, Colorado, over 100 km from the ERW. Due to terrain blockage, the KGJX misses much of the precipitation that

TABLE 1. A description of the instruments used in this analysis, along with their associated field campaign and physical location.

Campaign	Instrument	Location	Elevation
SPLASH	Dual-pol X-band radar	RJY 38°43′0.4794″N 106°51′10.44″W	2504 km MSL
SAIL	Dual-pol X-band radar	Mount Crested Butte 38°53′54.0996″N 106°56′35.304″W	3137 m MSL
SPLASH	OTT PARSIVEL disdrometer	KPS 38°56′31.2000″N 106°58′22.7994″W	2863 m MSL
		BCK 38°51′33.1200″N 106°55′15.2400″W	2723 m MSL
SPLASH	Surface meteorological instrumentation (thermometers, anemometers, etc.)	KPS BCK	
SAIL	Radiosondes	ARM site in Gothic 38°57′22.1688″N 106°59′16.2816″W	2886 m MSL

occurs in the watershed (Bytheway et al. 2024). Although the SPLASH radar had a better view of the ERW than KGJX, local terrain and trees near the radar site still created beam blockage issues for the radar at KPS and BCK. To reduce the impact of beam blockage in our analysis, a single azimuth of 342° was identified; this azimuth was closest to those of KPS (337.39°) and BCK (339.45°) but still maintained valid data at the lowest scan angle (4.0°) and reasonable coverage across its entire range. BCK-alternative (BCKa) and KPSalternative (KPSa) were defined as points along the 342° azimuth at the same range distance from RJY as KPS and BCK. Both alternative points are within 4 km of their original sites; based on knowledge of the sites and surrounding geography, these alternate locations do not introduce any significant differences to discussions of terrain influence, precipitation totals, or wind direction (Fig. 1). BCKa is 2718 m MSL, and KPSa is 2864 m MSL. Since the height of the lowest usable scan angle at the 342° azimuth is at least 300 m above the surface of each site, it is extremely unlikely that any surface snow processes (i.e., blowing snow) impacted radar data observations.

Observations from five main instruments were used in this study and can be found described in Table 1. SPLASH provided the primary data for this analysis, with SAIL used where necessary. For a complete list of additional SAIL instrumentation, see Feldman et al. (2023).

b. *Radar and disdrometer data*

The SPLASH and SAIL X-band radars were deployed for accurate precipitation observations to improve upon ground-based measurements by reducing the chance of wind interference and allowing a 3D picture of both particle structure and movement (Kumjian 2013a). The radars are dual-pol (i.e., polarimetric) systems, measuring horizontal reflectivity, radial velocity, spectral width, differential reflectivity, differential phase shift, linear depolarization ratio, and the copolar and cross-polar correlation coefficients (Kumjian 2013a). Both use a dual-pulse repetition frequency operating mode that increases the maximum unambiguous radial velocity value to ±33.5 m s^{-1} (Bharadwaj et al. 2010). This expanded velocity measurement range greatly facilitates the analysis of intense winter storms. Observation frequency is approximately 6 min for both types of X-band radar scans: plan position indicator (PPI) and range height indicator (RHI).

The SPLASH radar operates at a frequency of 9.4 GHz with a range resolution of 60 m, and elevation angles range from 1° to 15° above radar height. The radar is located at 2504 m MSL at the RJY site. The SAIL radar was deployed on the slopes of the Mount Crested Butte ski area at 3137 m MSL to provide detailed coverage over the ARM site (Fig. 1). The location afforded mostly unblocked views to the north of Mount Crested Butte, including the KPS site, but the radar experienced complete beam blockage to the south (ARM 2021a). A comparison of coverage of the most usable (6°) PPI scans from the SPLASH and SAIL radars is shown in Fig. S1 in the online supplemental material.

Two SPLASH OTT Particle, Size, and Velocity (PARSIVEL) disdrometers at KPS and BCK were used (Table 1). The disdrometers operate a horizontal laser that spans 180 mm between the parallel emitter and receiver and creates a measurement area of 54 cm^2 at a wavelength of 650 nm. By detecting the size and duration of any disruption to the laser, the disdrometers can measure the diameter and fall speed of precipitation in the size range of 0.2–0.8 mm with 32 particle size bins and 32 velocity classes (OTT Hydromet 2019). The data are collected every 2 min. The disdrometers are not wind shielded, creating the potential for effects of blowing snow and wind gusts on precipitation measurements.

c. *In situ meteorological data*

Surface wind and 10-m temperature data were collected at 1-min intervals at KPS and BCK. Surface precipitation gauge data were also available at both sites during the SPLASH campaign, but a power outage at BCK during the window of this event led to bridging, blocking the opening to the gauge, and thus the gauge data were not included in this analysis. Radiosondes were launched twice daily at 2330 and 1130 UTC from the SAIL site in Gothic, Colorado, at 2891 m MSL (Troyan 2013; ARM 2021b). These radiosondes were calibrated prelaunch, and surface temperature measurements have been compared to those taken at the lowest observable sonde level to ensure no significant biases or sonde artifacts (e.g., Sherwood et al. 2005). Air temperature, wind, equivalent potential temperature, and standard relative humidity with respect to water were the variables used in this analysis and were interpolated onto a time–height grid at 1-min resolution during preprocessing (Troyan 2013). Additionally, relative humidity with respect to ice was calculated using the Goff–Gratch equation (Goff and Gratch 1945; Dzambo and Turner 2016).

d. *Reanalysis data and atmospheric river identification*

The synoptic weather patterns were analyzed using 250-mb (1 mb = 1 hPa) wind speed and column-integrated water vapor transport (IVT) from ERA5 reanalysis data. ERA5 provides data products at a 9-km grid spacing and a 5-day latency window (Hersbach et al. 2020). The vector representation of IVT was created from the ERA5 variable "vertical integral of eastward (northward) water vapor flux" where the vertical integral is defined as from the (model) surface of Earth to the top of the atmosphere. AR occurrence was identified using the Guan and Waliser (2019) tracking algorithm applied to the three-hourly ERA5 IVT, using a 5° grid box centered on the ERW as the domain of interest. Cloud-top temperatures were obtained using the MODIS *Aqua*/*Terra* Cloud product, which indicates the atmospheric temperature at the top of the clouds measured in Kelvin with 5-km spatial resolution and daily temporal resolution (Platnick et al. 2017; King et al. 2003).

3. Methods

a. *Disdrometer precipitation estimates*

To understand whether significant differences in precipitation between KPS and BCK existed, disdrometer-estimated cumulative snowfall amounts in liquid-equivalent precipitation were examined over the event period and compared with particle size count. Four time periods with the most intense precipitation were identified using the cumulative disdrometer data and comparisons with other measurements of precipitation intensity (i.e., reflectivity, particle count). Time periods where the disdrometer did not correctly report at one or both sites were removed from the disdrometer dataset. A filter of 8 m s^{-1} was applied to correct for wind-induced effects per Capozzi et al. (2021). The median wind speed at KPS and BCK was 2.8 and 2.7 m s^{-1}, respectively, and so we assume that any wind-related biases the two disdrometers experience in relation to total precipitation measurements are similar. Despite this, noticeable variations in wind speed on smaller time scales do exist between the two sites.

Snowfall amounts were calculated according to methods listed in the OTT PARSIVEL disdrometer handbook and an OTT proprietary method of assuming variable particle density (OTT Hydromet 2024). Snowfall rates are determined using an algorithm proprietary to the disdrometer manufacturer from the particle count and drop size distribution (DSD). Any biases that may exist in these methods are assumed to be consistent between the two sites.

b. *Microphysical characteristics*

Microphysical characteristics of precipitation were examined using the horizontal reflectivity (Z_H), differential reflectivity (Z_{DR}), specific differential phase (K_{DP}), and cross-polarization correlation coefficient (ρ_{HV}) variables, calculated from the SPLASH X-band radar using the Python ARM Radar Toolkit (Py-ART; Helmus and Collis 2016). The Z_H (dBZ) was measured and used as a proxy for snowfall rate; high Z_H correlates with more intense snowfall (Kumjian 2013b). The Z_{DR} (dB) was measured and corrected by a factor of 0.245 dB for systematic bias using the method described in Oue et al. (2016). Additional bias may have been introduced during storm period 1 when it was possible that snow stuck to the radome, resulting in azimuthal Z_{DR} wedges from the beam passing through this addition to the radome surface. No attempt has been made to correct for wet radome attenuation effects (e.g., Frasier et al. 2013; Mancini et al. 2018). Positive Z_{DR} indicates horizontally oriented particles, and negative Z_{DR} indicates vertically oriented particles, while Z_{DR} near 0 indicates spherical particles (Kumjian 2013a). The K_{DP} (° km^{-1}) was calculated from the measured differential phase using the method described in Vulpiani et al. (2012) and is positively correlated with the density of a snow particle (Kumjian 2013a). The ρ_{HV} was measured and indicates the uniformity of the hydrometeors. For winter precipitation, ρ_{HV} values are usually very high (>0.9), although the presence of different crystal habits can produce minute fluctuations in ρ_{HV} values (Kumjian 2013b). As such, ρ_{HV} can be transformed into a visual proxy L to enhance small differences in the measurements using $L = -\log(1 - \rho_{\mathrm{HV}})$ (Helmus and Collis 2016).

Our analysis used traditional RHI scans and composite time series of the dual-pol variables at each field site were created using the radar gates closest to KPSa and BCKa, respectively. Vertical profiles of each of the four dual-pol variables were also generated from radar gates within 1.5 km of each site and averaged for a short time slice with intense surface precipitation. Temperature data from the SAIL radiosonde were overlaid on each site to show the height of the −15° and −5°C isotherm.

Quality control filters were applied to the radar data by removing data with a signal-to-noise ratio of <5 dB and a normalized coherent power of <0.5; these variables are important to radar filtering, and sensitivity testing was performed to derive these thresholds to ensure that they removed spurious artifacts while retaining echoes of interest (Chandrasekar et al. 2023). These filters reduced the quantity of SPLASH radar data displayed preferentially over KPS in figures utilizing RHI scans by filtering out partial beam blockage and significantly attenuated data. However, there is no evidence that the actual cloud depth at KPS was significantly different from BCK.

Additionally, the hydrometeor classification algorithm described in Bechini and Chandrasekar (2015) was applied to specific time slices after the Z_{DR} bias correction to check for consistency with assumptions of particle type from dual-pol signatures. Partial beam blockage can sometimes cause issues with the classification; this could have played a role given the complex terrain in the ERW. The various hydrometeor categories in our study build upon the prior work by Liu and Chandrasekar (2000), Dolan and Rutledge (2009), Chandrasekar et al. (2013), and Lim et al. (2013a,b). The dry snow (DS) and wet snow (WS) categories are a reference to the naming convention in Chandrasekar et al. (2013) but are synonymous with the dry and wet ice described in Bechini and Chandrasekar (2015). In this algorithm, the dry ice category has been found to indicate primarily aggregates and may also include lightly rimed particles (R. Bechini 2015, personal communication). The algorithm assigns the dominant particle type present in each region, which may prevent particles present for small spatial or temporal scales (e.g., dendritic crystals in our analysis) from appearing in the final hydrometeor classification results.

c. *Winds*

Surface wind data at 1-min intervals from anemometers at the meteorological stations were analyzed to provide a higher temporal resolution context for the radiosonde wind data. In addition, a standard dual-Doppler analysis was performed over this extremely complex terrain, utilizing both the SPLASH and SAIL radars. The SAIL and SPLASH radars are sufficiently close to perform this technique, but because they are directly in alignment with the valley (Fig. 1), only wind components in areas adjacent to the valley can be calculated, limiting analysis to specific times during which the two radars were oriented favorably. This analysis was performed using the National Center for Atmospheric Research (NCAR) Custom Editing and Display of Reduced Information in Cartesian Space (CEDRIC) technology based on theory by Armijo (1969) at scan angles ~4.8 km MSL (Miller 1998).

The wind vectors were calculated from two 4-min volume scans that started at the same time from each radar. For a given time slice, the perturbation wind vectors were calculated by creating a horizontal spatial average of all available u and v components of the wind vector at 4.8 km above MSL within the 40-km dual-Doppler grid extent, then subtracting this from the wind vector at a given location. This perturbation calculation follows established methods of using dual Doppler to diagnose wind patterns of widespread features such as those described in Kropfli and Kohn (1978) and Heymsfield (1979).

Radial velocity and spectral width datasets from the SPLASH radar were analyzed using the Py-ART Toolkit (Helmus and Collis 2016). Radial velocity is defined as the component of the hydrometeor velocity that is in the direction of the radar beam, and the dataset indicates the strength of this component, as well as whether it is toward or away from the radar (NOAA JetStream 2023). The radial velocity was filtered using a threshold of 0.8 applied to a velocity texture field calculated via Py-ART to reduce topography-induced artifacts (Helmus and Collis 2016). Spectral or spectrum width is a measurement of the dispersion of the radar beam due to wind shear, turbulence, or otherwise beam blockage (Doviak and Zrnić 1993).

4. Results and discussion

a. *Synoptic description and forcing mechanisms*

During the "Santa Slammer" period, four distinct episodes of moisture flux across the region occurred (Fig. 2). The four periods where significant snowfall occurred correspond with four periods of increased IVT into the region (Fig. 2) and with relatively higher column relative humidity observed in Gothic (Fig. 3a). The first and most impactful significant precipitation period occurred at 0300 UTC 24 December through 0000 UTC 25 December, hereafter referred to as storm period 1. Precipitation accumulations between 50 and 75 mm coincided with IVT over 300 kg $\mathrm{m}^{-1}\ \mathrm{s}^{-1}$ across western Colorado. An AR was present over the ERW from 0000 UTC 23 December to 0300 UTC 25 December (Fig. 2a). This AR had the strongest moisture flux observed over the entire analysis period, the likely cause of storm period 1's relatively deeper storm, which was indicated by deep radar echo tops and cloud-top temperatures below 220 K. This period also contained a double vertical maximum of high relative humidity values (Fig. 3a), indicating a potential dry layer (e.g., see Rea et al. 2023). The AR was preceded by a shallow warm frontal system passage, indicated by tight equivalent potential temperature contours between the surface and roughly 3.3 km above MSL in Figs. 3a and 3b and the sharp surface temperature increase observed for the first 24+ h of the study period, shown in Fig. 3c. However, the AR precipitation event itself took place during a near-surface air temperature decrease (Fig. 3c), suggesting it was closely tied with the cold frontal passage (Neiman et al. 2013; Rutz et al. 2014). Average temperatures during storm period 1 were the warmest of the entire analysis period, briefly reaching above freezing at both field sites around 0400 UTC 24 December, resulting in extremely wet and dense precipitation as noted by local weather observations (CoCoRAHS 2021). Precipitation recorded with the disdrometer was significant (storm period 1 in Fig. 4a), especially during the latter half of the window, with accumulations between 25 and 50 mm and a large range of particle sizes, with consistent records of hydrometeors 4–6 mm in diameter—consistent with impacts of an interior continental AR event (Rutz et al. 2014).

During this time, the ERW was also located near the right entrance region of a jet streak, as seen in the 250-mb contours in Fig. 2a. This location indicates a synoptic forcing of divergence aloft and convergence at the surface, creating favorable conditions for cloud formation and precipitation over this region. Surface winds during storm period 1 were consistently aligned with the valley (southwesterly at BCK and southeasterly at KPS), with median surface speeds of roughly 4.5 m s^{-1} observed at both sites (Fig. 5). Directional shear was observed

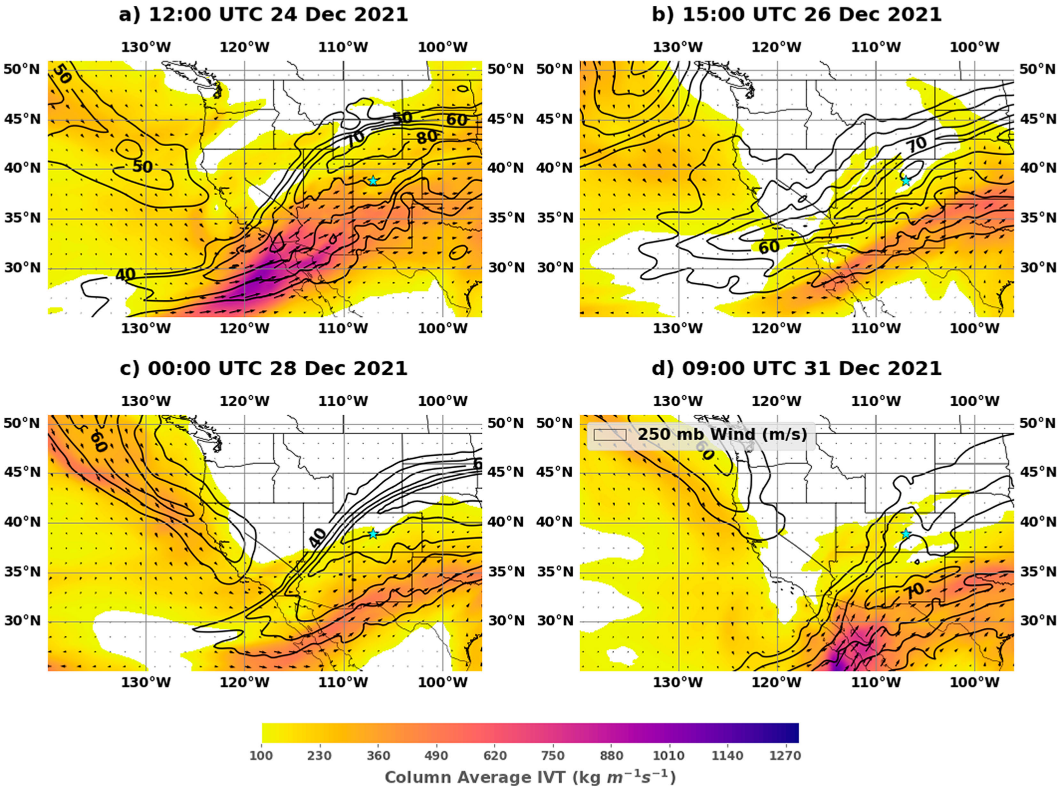

FIG. 2. Snapshots at the time of maximum column average ERA5-Land IVT (color bar) for the western United States during the four distinct precipitation periods. Arrows represent the IVT vectors. The 250-mb wind (m s^{-1}) in 10 m s^{-1} intervals is denoted by the black contours. The cyan star shows the location of the ERW in western Colorado.

along the radial velocity axis, and boundary layer shear can be concluded from wind and stability profiles (Fig. 6).

Following storm period 1, there was a significant drop in atmospheric moisture over the region, with a shallow cold pool present over the SAIL site (Fig. 3a). Then, beginning around 2200 UTC 25 December, a narrow but extremely strong cold frontal passage was observed by surface meteorology stations, though largely missed by the interpolated radiosonde data. The temperature climbed rapidly again within 12 h, likely indicating a subsequent warm front, and then dropped again slowly over the remaining 12 h of 26 December (Fig. 3b). This last drop in temperature was accompanied by another period of intense precipitation at both KPS and BCK (Fig. 4), defined as storm period 2 (Fig. 4a) from 1200 UTC 26 December until 0000 UTC 27 December. Storm period 2 was also associated with increased IVT over western Colorado related to a second AR over the ERW, which took place from 0000 UTC 26 December to 2100 UTC 26 December. Surface temperature trends suggest storm period 2 was associated with another cold frontal passage (Neiman et al. 2013; Rutz et al. 2014; Houze 2012) but with warmer cloud-top temperatures between 245 and 250 K.

Roughly 25 mm more precipitation was recorded at BCK than at KPS during storm period 2. A short window of high particle counts was observed at BCK and a longer, but less intense window was observed at KPS (Figs. 4b,c). Surface wind speeds were high, with median values of 7.5 m s^{-1} at BCK and 5.6 m s^{-1} at KPS, but in contrast to other storm periods, storm period 2's radial winds exhibited little evidence of valley-parallel winds (Fig. 6b). Light precipitation continued throughout 27 December as the temperature steadily decreased.

Around 1200 UTC 27 December, temperature increased rapidly (Fig. 3b), and a slight tightening of the equivalent potential temperature lines is seen, likely indicating the passage of a shallow warm front, followed by a temperature decrease over the last 12 h of 27 December. Around this time, another period of high IVT was observed in the region (Fig. 2c), which was associated with a third AR that took place from 1200 UTC 27 December to 0300 UTC 28 December. This AR event and associated cold frontal passage observed in Fig. 3c overlapped with cooler cloud-top temperatures between 235 and 245 K and a window of high precipitation amounts, defined as storm period 3 from 0000 to 1200 UTC 28 December (Fig. 4a).

During storm period 3, there appeared to be slightly more precipitation at KPS, with larger particles at KPS and higher counts of small particles at BCK. This was associated with another period of increased surface wind speeds, with median values of 4.4 m s^{-1} at BCK and 4.9 m s^{-1} at KPS (Fig. 5a). However, surface winds were in a variety of directions (i.e., up-valley, cross-valley, and down-valley over this 12-h period,

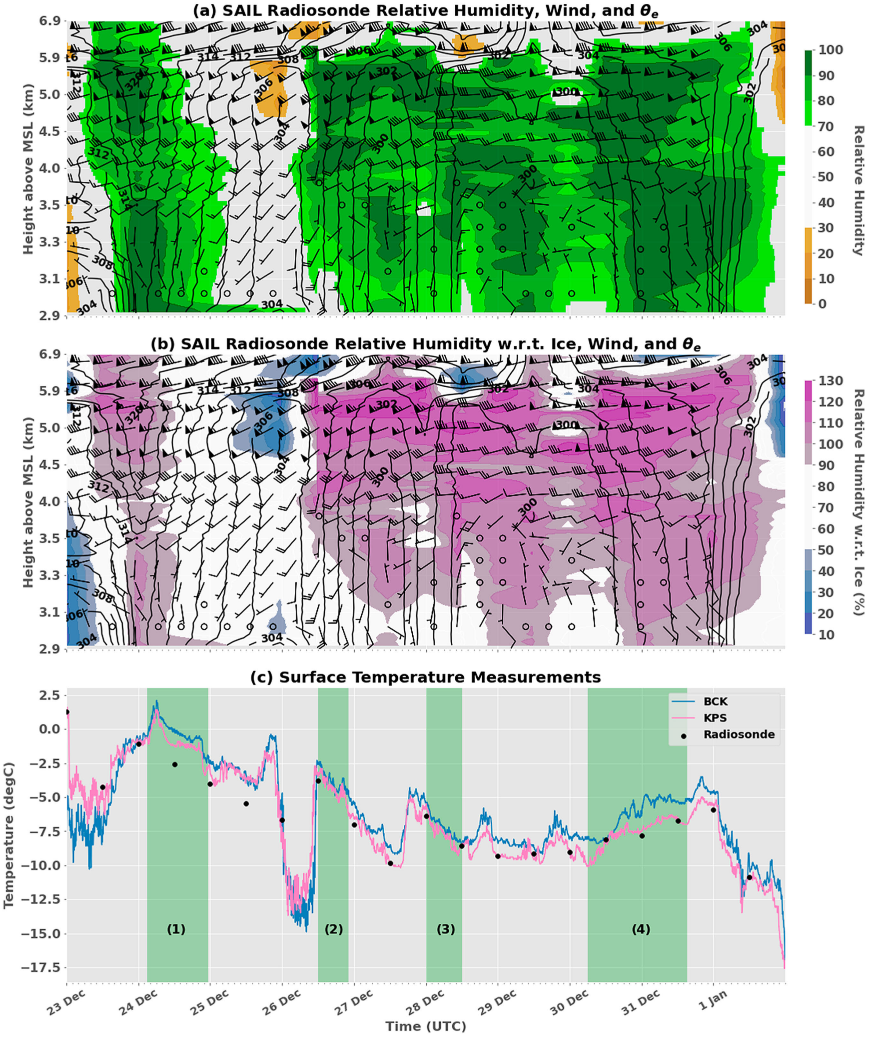

FIG. 3. (a) SAIL interpolated data from radiosonde launched at 0000 and 1200 UTC from Gothic, showing relative humidity via the color bar, equivalent potential temperature (K) via the black contours, and wind barbs representing wind speed and direction (with the time stamps for IVT analysis in Fig. 2 denoted by arrows along the *x* axis); (b) as in (a), but using relative humidity with respect to ice; and (c) over the same time frame, depicts the surface air temperature at BCK and KPS measured in 2-min increments with the radiosonde surface air temperature data represented by black dots. Storm periods 1–4 are denoted by the green shading and represent four distinct periods of precipitation within the analysis period.

with the median values being southeasterly at BCK and west–north westerly at KPS), and no obvious radial velocity patterns emerged (Fig. 5c), although boundary layer shear was observed (Fig. 6c).

The temperature at both sites remained steady between −5° and −10°C from 1200 UTC 28 December through 0000 UTC 1 January, when it again rapidly dropped. In this instance, the precipitation window was more centered in the warm sector ahead of the cold front; storm period 4 can be defined as 0600 UTC 30 December through 1600 UTC 31 December (Fig. 4a). Storm period 4 was associated with the final push of IVT into western Colorado (Fig. 2d) and overlapped with the fourth and final AR, which took place from 2100 UTC 30 December through 0900 UTC 1 January. Based on temperature patterns, this storm period can be classified as more prefrontal on the surface as compared to the other three storm periods. It was also associated with cooler cloud-top temperatures again, around 230 K. This storm period's precipitation exhibited the most significant differences between the two sites, with much higher counts of particles recorded at BCK, especially in the 0.5–1-mm range, and an overall greater increase in cumulative precipitation at BCK as compared to KPS. Surface wind observations were primarily up-valley (southeasterly at KPS and southwesterly at BCK), indicating potential for upslope flow (Fig. 5b). However, they were overall weak, with median speeds of 3.5 m s^{-1} at BCK and

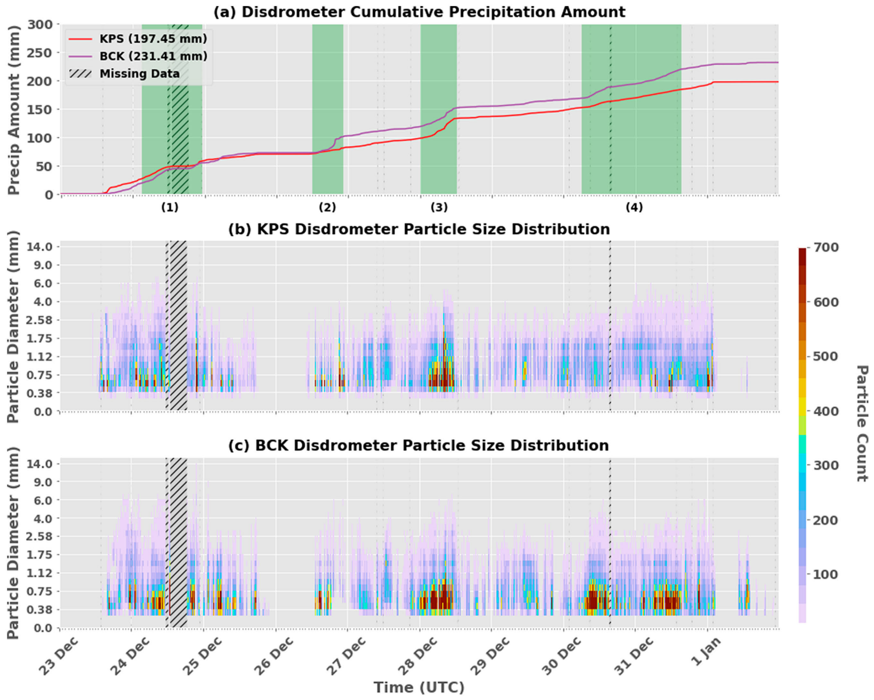

FIG. 4. (a) Disdrometer cumulative precipitation amount at BCK (purple) and KPS (red). Missing data are identified with a hatched symbol (i.e., gray background and black diagonal lines). (b),(c) Disdrometer particle size distribution, with particle count denoted by the color bar and diameter (mm) on the y axis, for KPS and BCK, respectively. Storm periods 1–4 are denoted by the green shading and represent four distinct periods of precipitation within the larger event.

1.7 m s^{-1} at KPS, which are at or below the whole time-period average (Fig. 5a). Radial velocity patterns indicated directional wind shear along the valley axis, and stability and wind profiles reveal boundary layer shear (Fig. 6).

On a synoptic scale, each of the storm periods was induced by a distinct AR passage associated with the transition from a warm sector to a cold frontal region of a midlatitude cyclone. This supports the conclusion that the period from 23 December to 1 January should not be considered as one uniform event, but rather several distinct events marked by frontal passages, each with the potential for unique microphysical characteristics. It is relevant to note that the first three events were prefrontal in nature, leading to the expectation of some similar characteristics, including a relatively stable atmosphere, uniform radar echo tops, and the potential for enhanced precipitation on the windward side of orography (Zagrodnik et al. 2019; Geerts et al. 2015; Medina and Houze 2015; Aikins et al. 2016). In addition, the observation of boundary layer shear through surface and lower atmosphere analysis in all four storm periods may be a forcing mechanism for turbulence and precipitation, as suggested in previous publications (Geerts et al. 2015; Medina and Houze 2015); this is discussed further in following sections.

b. *Wind analysis*

To take a more in-depth look at the potential for orographic enhancement, we next examine observed winds. Near-surface flow in inner mountain valleys, such as the East River Valley, often experiences relative isolation with respect to the synoptic wind flow, caused by mechanisms including local orographic blocking and terrain-influenced decoupling of the surface boundary layer (González et al. 2021; Gonzalez et al. 2019; Tessendorf et al. 2019; Medina et al. 2005; Campbell and Steenburgh 2014). Near-surface wind at the two sites (Fig. 5) is of relatively consistent magnitude (Fig. 5a), with a median wind of 2.8 m s^{-1} at KPS and 2.7 m s^{-1} at BCK; the median wind at KPS was southeasterly (~136°), while the winds at BCK were southwesterly (median of ~220°) (Fig. 5b). These wind directions demonstrate that flow at both sites is, in general, parallel to and dominated by the direction of the main valley axis, consistent with González et al. (2021). Near-surface winds perpendicular to the prevailing flow and parallel to local terrain are a common indication of orographic blocking (e.g., Abel et al. 2009; Neiman et al. 2013; Kingsmill et al. 2013; Marwitz 1987). However, conclusively diagnosing orographic blocking in the ERW is fraught by the region's exceptionally complex terrain—which makes diagnosing an effective barrier height challenging—and our limited observations, which do not include any measures of stability upstream (i.e., west) of the ERW. In addition, there is no indication of a low-level jet that would indicate sustained orographic blocking (e.g., the Sierra Barrier jet; Kingsmill et al. 2013; Neiman et al. 2013).

To get a more detailed understanding of wind patterns over space and time and potential impacts of stability, Fig. 6 shows

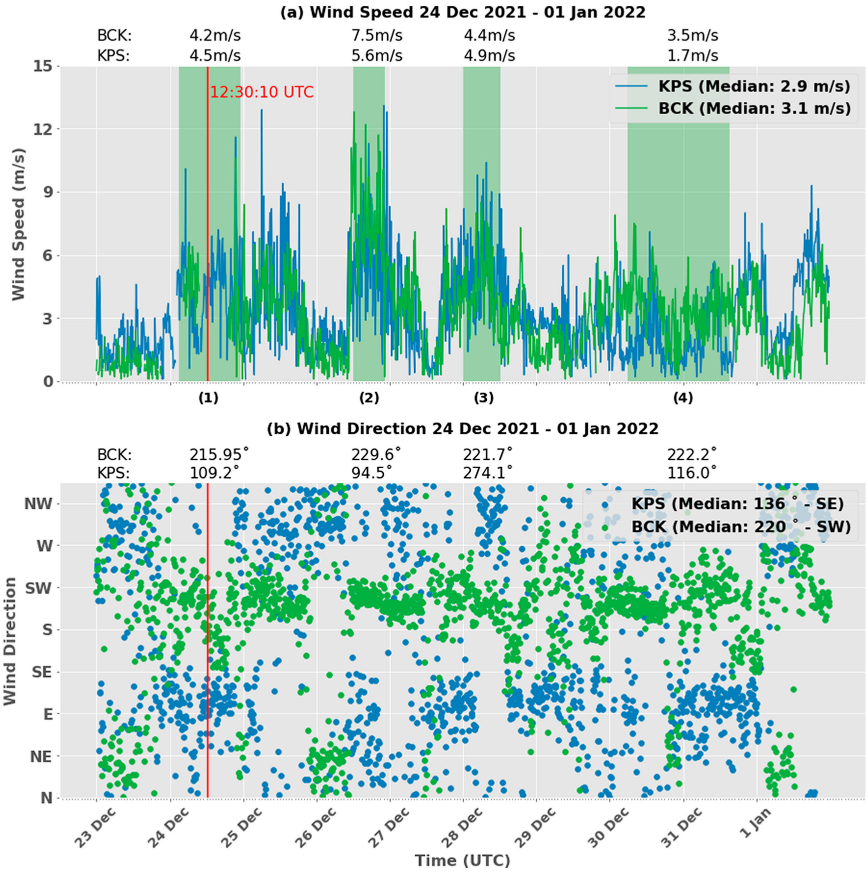

FIG. 5. (a) Wind speed at 10-min intervals. The median values recorded at each site are displayed in the upper-right corner legend. KPS data are the blue line, and BCK data are the green line. Storm periods 1–4 are denoted by the light green shading and represent four distinct periods of precipitation within the analysis period. (b) Wind directions represented by blue dots for KPS and green dots for BCK, also at 10-min intervals. The median direction at each site is displayed in the legend. A standard conversion chart was used to convert wind direction from degrees to cardinal directions. The time analyzed in Fig. 8 is denoted by the red line. Median values for each storm period are shown above the respective subfigure.

the average radial velocity from RJY and time-mean wind barbs and potential temperature profiles (equivalent potential temperature shown in Fig. S2) from radiosondes released at Gothic. Profiles of potential temperature are displayed to give a sense of atmospheric stability. Radial velocity is relatively weak over KPS and BCK, where there are depressions in the terrain, and the observed near-surface wind at Gothic is also relatively stagnant under stable conditions at many times (Figs. 3 and 6). These observations could indicate local orographic blocking, and this in turn may have helped generate local shear (Abel et al. 2009; Medina and Houze 2015; Medina et al. 2005; Marwitz 1987). Winds at the lowest levels above KPS (~25 km from radar) also exhibit a small negative radial velocity component (i.e., toward the radar), consistent with the time-mean wind direction and radiosonde wind profiles, indicating a northeasterly wind, i.e., with a component down-valley (Figs. 5 and 6b,c). BCK generally experiences small to near-zero radial velocities directly overhead, consistent with west-southwesterly winds observed at the surface stations, which are nearly perpendicular to the RHI azimuth at BCK (Figs. 5 and 6).

Meanwhile, a shallow region of outbound radial velocity is seen extending from the radar to Mount Crested Butte, near BCK (Fig. 6), indicating that the side closest to the radar is generally the windward side. The time-mean potential temperature profiles provide a proxy for stability and exhibit near-neutral stability, likely indicating a shallow boundary layer, between the surface and ~4 km MSL. Above ~4 km MSL, a noticeable increase in the potential temperature lapse rate coincides with directional and speed shear in the wind profiles for all four storm periods. Directional shear is observed in radial velocity from 0 to 30 km in range of RJY during storm periods 1 and 4 (Fig. 6), with winds pointed first away, then perpendicular, then directly inbound to the radar (~4.5 km MSL) from near-surface to aloft, at mean speeds up to $-5\ \mathrm{m\ s^{-1}}$ (Figs. 6a,d). This shear layer is sloped slightly upward toward the region of higher orography further away from the radar.

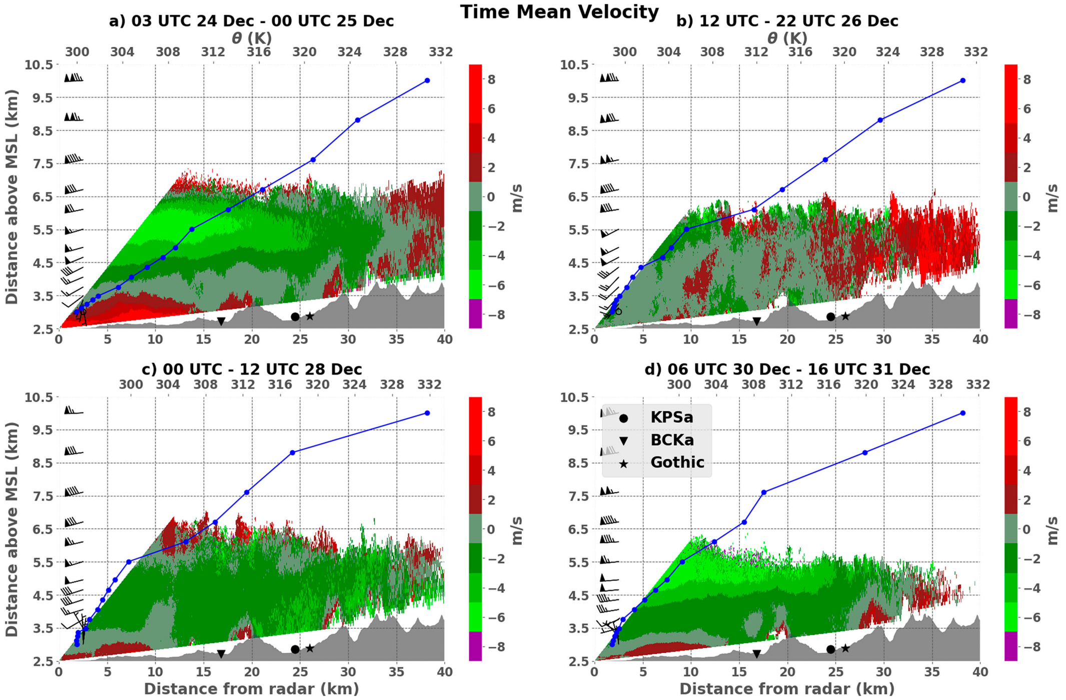

FIG. 6. Time-mean radial velocity 342° azimuth RHI scans from SPLASH radar during the four storm periods. The triangle marker denotes the BCKa site, and the circle marker denotes the KPSa site. Origin is the location of the RJY site. Red represents winds away from the radar, and green represents winds toward the radar. Given the orientation of the RHI scan, red (green) colors indicate wind patterns that are aligned with the valley away from (toward) the radar, while the gray color represents a radial velocity of zero, indicating cross-valley winds or still conditions. The blue line shows the time-mean potential temperature profile (K) (see x axis at top of each subfigure) for each storm period from the ARM radiosonde launched at Gothic; wind barbs are time mean and also from the radiosonde.

Figure 7 provides an understanding of how winds above the surface behave by displaying horizontal wind vectors corresponding to 1230 UTC 24 December, a period of intense precipitation during storm period 1 (Fig. 4a). Figure 7a shows that when the surface wind at KPS is southeasterly and at BCK is southwesterly (i.e., corresponding time in Fig. 5), the winds at 4.8 km MSL (i.e., above the height of the regional topography) are completely southwesterly and strong, at roughly 40 m s^{-1}. These winds are aligned with the upper-level winds (which correspond with the synoptic-level flow at 250 mb, Fig. 2a) consistent with González et al. (2021). Meanwhile, Fig. 7b displays the spatial perturbation wind at 4.8 km, indicating enhancement of cross-valley winds.

Meanwhile, Fig. 8 shows spectral width as a proxy for turbulence, which for all four time periods is enhanced below 4.5 km MSL, indicating increased turbulence. Spectral width is specifically enhanced over and slightly upstream of Mount Crested Butte (~20 km from the radar along the horizontal axis in Fig. 8) and over the topography northeast of the mountain along the azimuth. The pattern enhancement is seen strongly over BCK but does not always extend upstream to KPS. This is consistent with the radial velocity patterns (Fig. 6), since as noted above, KPS featured northwesterly winds inbound to the radar during these times (i.e., downslope, not upslope).

c. *Surface snowfall analysis*

In situ disdrometer-observed precipitation (Fig. 4) exhibits periods where significant snowfall occurred over short periods of time and other periods where little to no precipitation occurred; these significant precipitation events generally corresponded to higher counts of small particles at the surface, as well as larger range of particle diameters (Figs. 4b,c). Out of all the disdrometer measurements, the calculated snowfall rates have the strongest and most linear relationship with particle count (not shown), indicating that high particle counts are likely the primary driver of the high snowfall rates observed within each of the storm periods, especially storm periods 2 and 3, where very high relative counts are observed (Fig. 4). This size distribution is also consistent with results by Shen et al. (2022) which found that higher intensity snowfall was generally associated with higher particle counts of smaller diameters. Given that the temperature at the surface was generally below freezing and the windows of high particle counts seen in Figs. 4b and 4c were primarily observed to range in diameter between 0.5 and 1 mm, it can be inferred that the particles most likely to be responsible for these high count periods can be classified as ice crystals (Bechini and Chandrasekar 2015; Dolan and Rutledge 2009). Despite high counts of small particles, observed droplet size distributions included particles

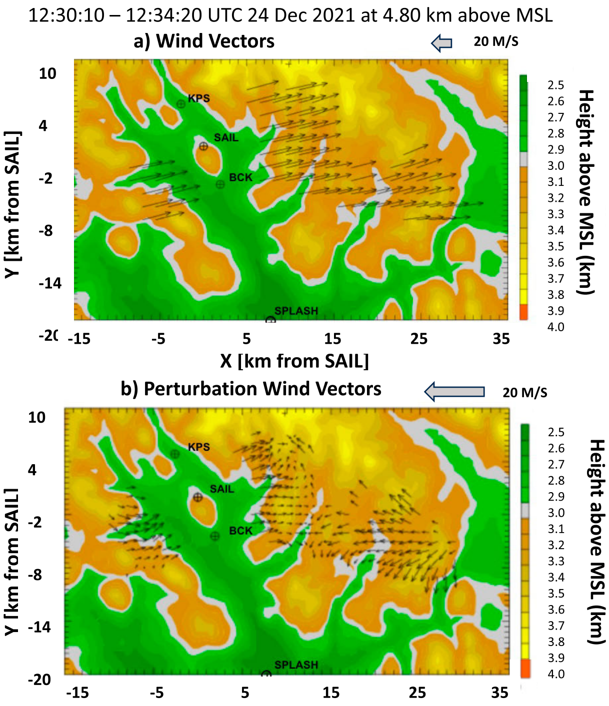

FIG. 7. (a) Average wind speeds from SPLASH and SAIL radar data starting at 1230:10 UTC using dual-Doppler analysis. (b) Perturbation winds during the same time step after subtracting the mean *u* and *v* components. Color shading represents topography (km).

measuring as large as 6 mm in diameter, which hydrometeor classification defines as aggregates (Dolan and Rutledge 2009; Bechini and Chandrasekar 2015). Storm period 1, which had the warmest overall surface temperatures (Fig. 3c) was observed to have the largest disdrometer drop size distribution. This is supported by Fig. 9, where it is clear that drop size distributions of 10 mm or greater were found most frequently during storm period 1 at both sites and only during storm period 1 at KPS. Drop size distributions were also found to be generally higher during each of the storm periods than during the remainder of the analysis window (Fig. 9). Furthermore, the width of the observed drop size distribution was found to exhibit a positive relationship to air temperature, consistent with Yin and Yuan (2022) (Fig. S3).

Time-mean reflectivity (Z_H; Fig. 10) generally shows enhancement of reflectivity over topography, with specific enhancement on the windward (south) side of Mount Crested Butte and over the orography to the northeast of KPS. This enhancement is most prominent in Fig. 10a, where the deeper column of magnitude 20 dBZ begins on the windward side over the BCK site and continues slightly downstream; the same phenomenon is seen downstream of KPS. This contrast over the two sites supports disdrometer observations that show more intense precipitation at BCK during this time and indicates that an orographic forcing mechanism was responsible for this spatial variability. Meanwhile, Z_H on the windward side of Mount Crested Butte is enhanced upstream (down-valley) of the BCK site (Figs. 10a–c), generally consistent with outbound radial velocity (Fig. 6) detected at low levels in this region and indicating orographic upslope forcing.

d. Microphysical and particle analysis

To better understand the particle formation mechanisms that generated the observed variability in surface snowfall, we next examine the time evolution of radar-observed dual-pol variables at each site (Fig. 11). Each storm period had its own unique microphysical characteristics. Dual-pol variables and their variability with height can help determine these characteristics, such as crystal type and structure. Storm period 1

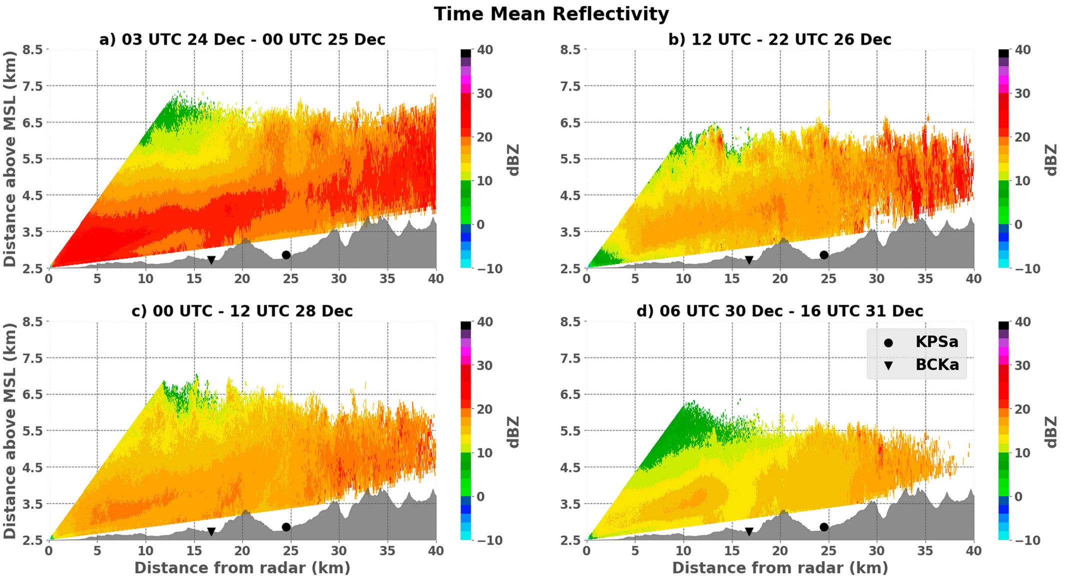

FIG. 8. Time-mean horizontal reflectivity over the four storm periods along the same azimuth as shown in Fig. 6. The BCKa and KPSa site locations are denoted by the black upside-down triangle and circle, respectively.

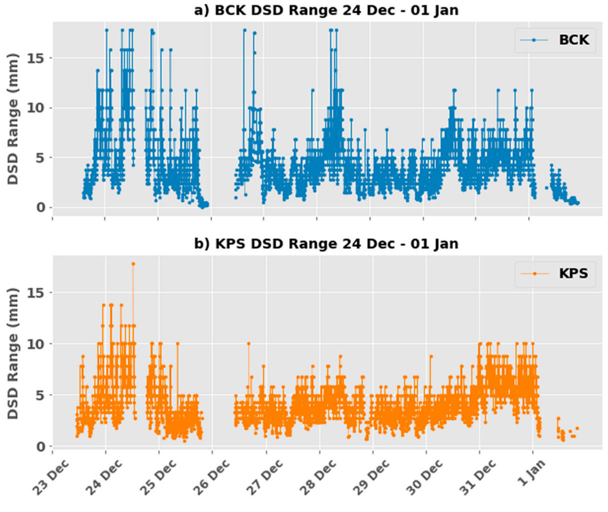

FIG. 9. Time-series plot showing the DSD range (particle diameter maximum − minimum) recorded by the disdrometer at 2-min intervals over the analysis period for (a) BCK and (b) KPS.

best illustrates this in terms of Z_H, Z_{DR}, and ρ_{HV} characteristics; for instance, dendritic crystal growth via diffusion is known to occur in general proximity to the −15°C isotherm, where diffusional growth speeds are maximized (~5 km MSL during storm period 1) (Bailey and Hallett 2009; Bechini et al. 2013; Rogers and Yau 1989). Evidence for this is seen in storm period 1 at both KPS and BCK around and above the −15°C isotherm: Z_{DR} was at a maximum, with 1-dB values, and K_{DP} was also large in magnitude, with values around 2.5 km^{-1}. Meanwhile, ρ_{HV} and Z_H exhibited relative minimums. Evidence of this signature can also be seen in instantaneous vertical profiles of dual-pol variables between the −15° and −5°C lines in Fig. S4. This enhancement of Z_{DR} and K_{DP} and slightly decreased ρ_{HV} represents a dual-pol signature commonly associated with planar or dendritic crystal growth, i.e., pristine ice crystals undergoing growth via vapor deposition (Kumjian 2013b; Bechini et al. 2013). The presence of pristine ice crystals above 5 km MSL is confirmed by the hydrometeor identification shown in Fig. 12a. This signature is correlated with increased precipitation recorded at the surface by the disdrometer, seen in Fig. 4a in agreement with Bechini et al. (2013), who found a strong correlation between K_{DP} enhancement at the −15°C isotherm and surface precipitation unique to stratiform precipitation.

However, below 4.5 km, the dual-pol variables displayed opposite trends. The Z_H increased to 20 dBZ, and ρ_{HV} increased above 0.98 ($L = 2$), while K_{DP} and Z_{DR} were on average much lower, i.e., 1° km^{-1} and 1 dB, respectively. This is consistent with aggregation processes beginning to dominate closer to the surface (Kumjian 2013b; Allabakash et al. 2019). Specifically, the negative correlation between Z_H and Z_{DR} indicated that the particles were becoming larger and more isotropic, and lower K_{DP} and Z_{DR} magnitudes suggested the presence of low-density particles. In short, the dual-pol variables suggest large low-density aggregates, consistent with surface observations, hydrometeor classifications (Fig. 11a), and similar signatures observed in Allabakash et al. (2019). These results are also consistent with Brandes et al. (2007) who found that low-density aggregates become more frequent at temperatures above −5°C and at humidity above 95%, conditions which were present at 1.5 km above the surface and below during storm period 1 (Figs. 3b,c). The small values of Z_{DR} in the layer just above the surface are likely a result of mixed particle shapes, including the presence of both small crystals and aggregates; this pattern is consistent with known

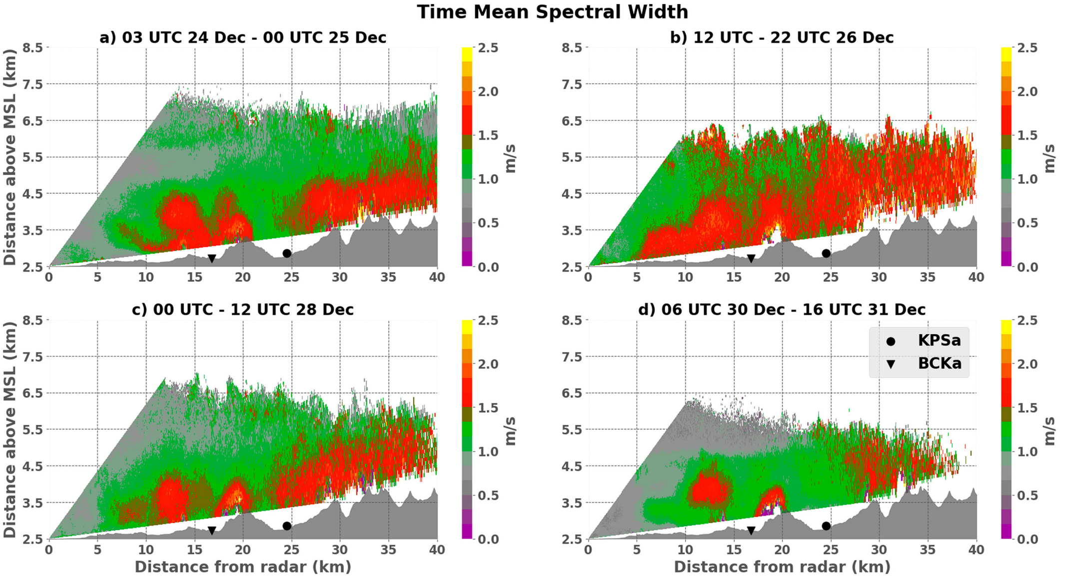

FIG. 10. Time-mean spectral width RHI scans over the four storm periods along the same azimuth as shown in Fig. 6, with the KPSa and BCKa sites denoted by the black upside-down triangle and circle, respectively. Velocity dealiasing was applied to the data.

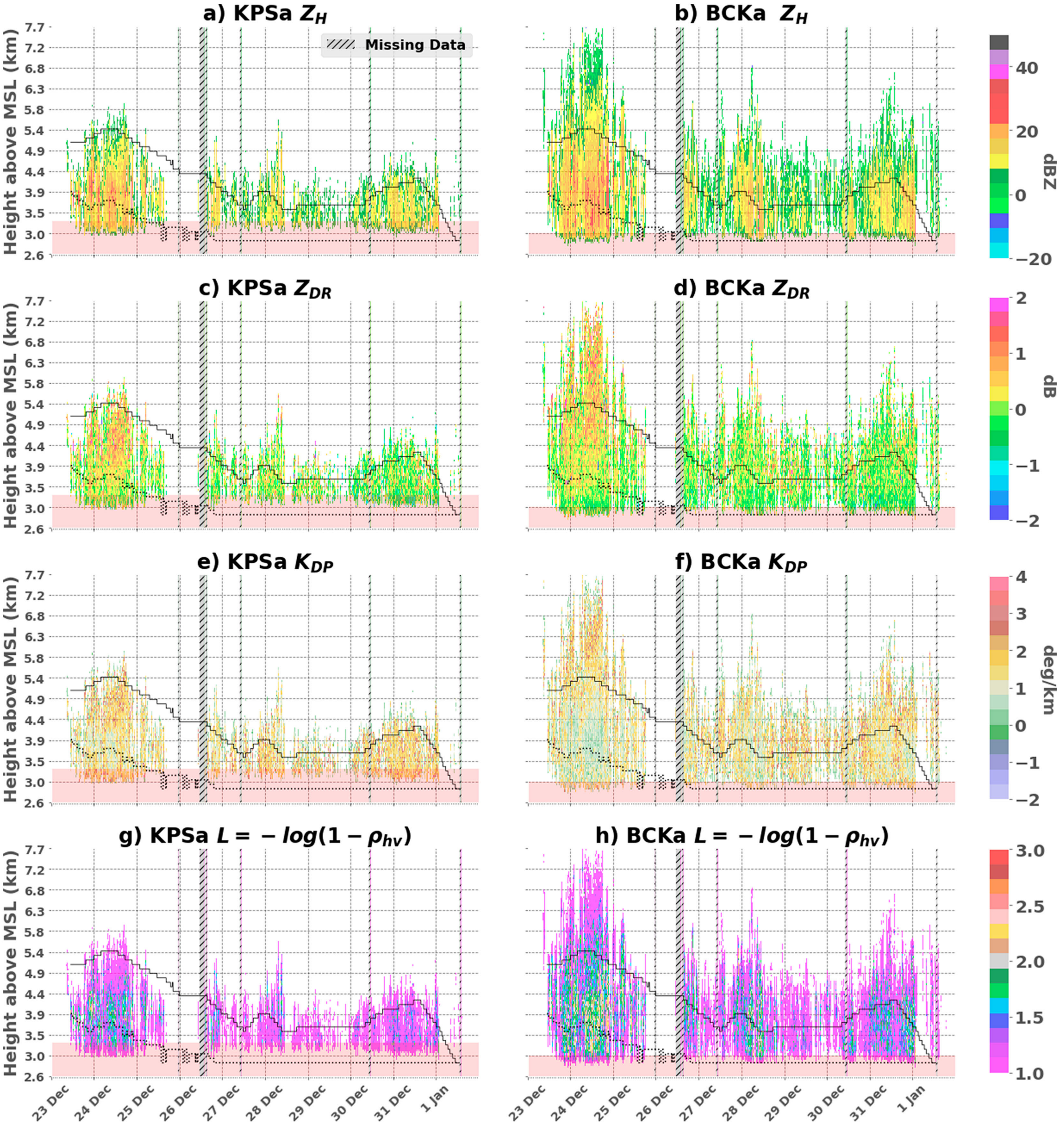

FIG. 11. Time–height profiles derived from RHI scans at the 342° azimuth from SPLASH radar at the radar gate above (left) KPSa and (right) BCKa. (a),(b) Horizontal reflectivity Z_H (dBZ); (c),(d) differential reflectivity Z_{DR} (dB); (e),(f) specific differential phase K_{DP} (° km^{-1}); and (g),(h) L, a proxy for the cross-polarization correlation coefficient (ρ_{HV}). Note that as the coefficient increases, L increases. The solid (dotted) black line denotes the −15°C (−5°C) isotherm, derived from the radiosonde data. The red shading denotes the areas where data were filtered out due to possible partial beam blockage. Missing data are shown in hatch markings.

particle types often found at the colder atmosphere temperatures observed during this period (Nguyen et al. 2019; Yin and Yuan 2022). Furthermore, this combination of particle growth mechanisms is consistent with disdrometer particle size observations (Figs. 4b,c) which recorded high counts of small ice particles within the size range of crystals reaching the surface at all time periods but also recorded some larger aggregates during all storm periods, with especially large aggregates and a large range in drop size distribution observed during storm period 1 (Figs. 4 and 9).

The observed vertical variations in the dual-pol signatures during storm periods 2–4 (Fig. 10), though weak, are consistent with pure crystals (CR in Fig. 12) growing via diffusion in upper levels and light particle aggregation (DS in Fig. 12) at lower levels. This is confirmed by the hydrometeor classifications shown in Fig. 12 (Bechini and Chandrasekar 2015). However, based on the reduced area of the category observed in the RHI scans, there was less particle aggregation (DS category) observed during these latter three periods than in storm period 1. It was also observed that during storm periods 2–4, disdrometer precipitation totals were lower than during storm period 1 (i.e., <60 mm), i.e., the disdrometer did not pick up as many counts of particles larger than 2.5 mm in diameter as observed in storm period 1 (Allabakash et al.

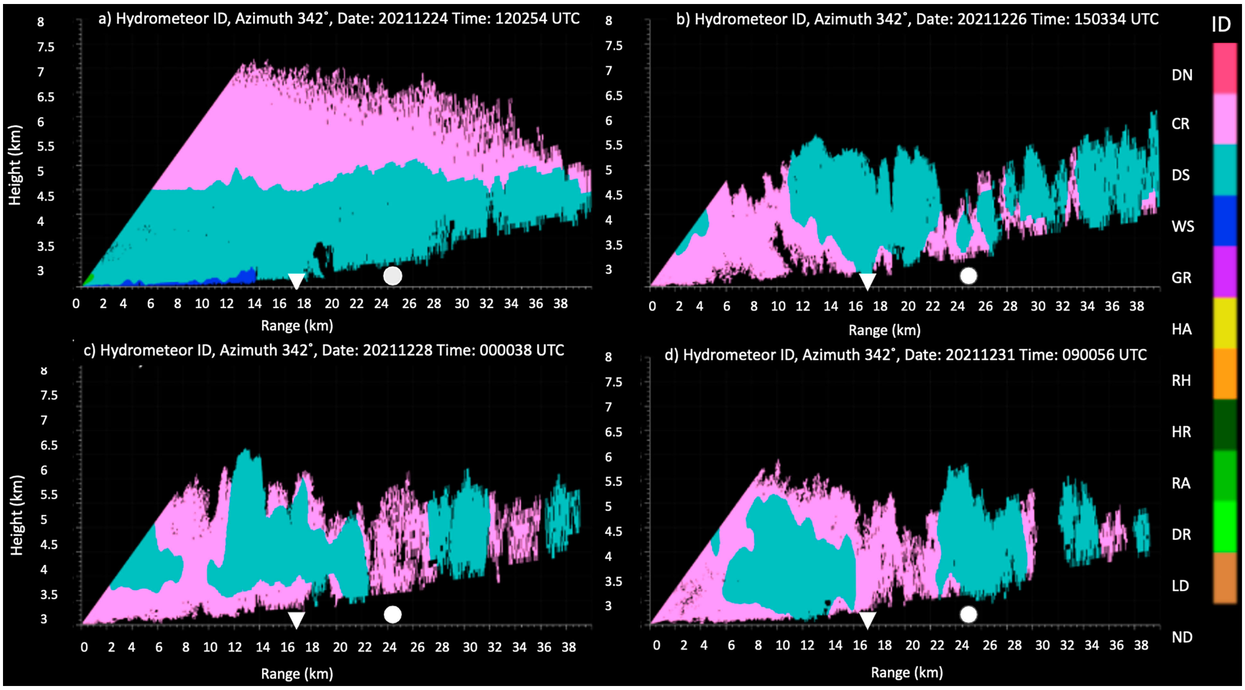

FIG. 12. RHI scans along 342° azimuth from SPLASH radar created using the hydrometeor ID algorithm discussed in the text. (a)–(d) Example time slices in previously identified storm periods 1–4, respectively. BCK is at roughly 17 km, and KPS is at 24 km. Classifications include CR (pink), DS (turquoise), and WS (dark blue). The BCKa and KPSa site locations are denoted by the white upside-down triangle and circle, respectively.

2019; NOAA Virtual Lab 2022). This is consistent with the air temperatures being relatively cooler during these storm periods (i.e., the −5°C isotherm is at the ground). Previous research has shown that temperatures less than −5°C at particle formation height tend to be associated with a smaller hydrometeor size range, while temperatures above −5°C are dominated by aggregation and larger hydrometeors (Brandes et al. 2007; Yin and Yuan 2022).

In addition, evidence of generating cells, a source of initial ice growth in the seeder–feeder process (i.e., the seeder region), existed in all storm periods, with particularly strong evidence of the streaks of enhanced Z_H at the top of the radar echo that are a signature of this process during storm period 1 (Fig. S5 and Fig. 11; Douglas et al. 1957; Ramelli et al. 2021; Keeler et al. 2017). Because the cells are small (∼1 km), the analysis of RHI scans from a single azimuth likely underrepresents their occurrence (Kumjian et al. 2014). Previous publications have found that ice formation and growth are enhanced within these generating cells, and specifically, cells with large Z_H and low Z_{DR} can indicative dendrites growing at large supersaturations, increasing their likelihood to aggregate and form isotropic particles; this is potentially a contributor to the large particle sizes and high precipitation rates observed through all storm periods but especially storm period 1 (Houze et al. 1976; Kumjian et al. 2014; Ramelli et al. 2021; Geerts et al. 2015). Consistent with Fig. 6, generating cells are often induced due to weak instability generated from ascent over an orographic barrier and are typical in cases even when the stability profile is approximately neutral in the boundary layer (Geerts et al. 2015).

The differences between storm period 1 and the other three storm periods may be further explained by the fact that the deeper cloud layer and warmer temperatures during storm period 1 allowed more time for growth via aggregation in the lower atmosphere, where temperatures ranged between −15° and 0°C (Yin and Yuan 2022; Brandes et al. 2007, Figs. 4 and 9, and Fig. S3). The deeper cloud layer allowed for particle formation to take place at levels relatively higher in altitude, where temperatures were below −15°C, conditions favorable to the depositional growth of ice crystals (Yin and Yuan 2022; Rogers and Yau 1989). Some proportion of these crystals were likely able to reach the surface because aggregation often affects only a portion of the air column, and a mix of both particle types reach the surface as can be seen in the wide range of disdrometer particle sizes observed at both sites in Figs. 4b and 4c; this is common at temperatures around 0°C (Yin and Yuan 2022). An additional explanation considered for the high snowfall rates (Fig. 4a), small particle counts (Figs. 4b,c), and elevated reflectivity (Figs. 8a and 11a,b) observed in storm period 1 was secondary ice production since the −5°C isotherm was reasonably high above the surface. However, since there is no evidence of riming processes or graupel in the dual-pol variables of Fig. 11 (i.e., no negative Z_{DR}) or the hydrometeor classification algorithm in Fig. 12, this is unlikely to be a relevant mechanism during this period (Kneifel and Moisseev 2020).

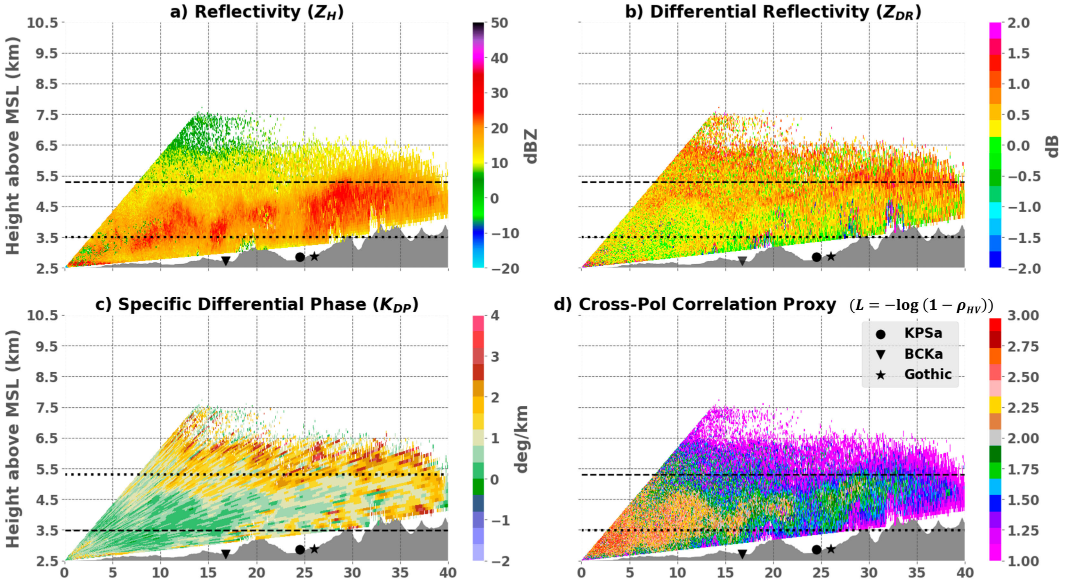

FIG. 13. RHI scans along the 342° azimuth from SPLASH radar displayed for each of the four dual-pol variables at 0814:46 UTC 24 Dec 2021 (during storm period 1). The BCKa, KPSa, and Gothic site locations are denoted by the black upside-down triangle, circle, and star, respectively. The dashed (dotted) black line indicates the −15°C (−5°C) isotherm, derived from sounding launched at Gothic. The isotherms, derived from the radiosonde launched at Gothic, are displayed at a constant height on the RHI even though in reality isotherms often slope within complex terrain (e.g., Minder et al. 2011).

Figure 13 demonstrates a time slice from 0814 UTC 24 December 2021 that helps emphasize the conclusions reached about storm period 1 from Fig. 11. For instance, the bands of enhanced Z_{DR} and K_{DP} and the ρ_{HV} depression at upper levels (i.e., at or above the −15°C isotherm) can be seen clearly in Fig. 13. As discussed above, previous studies have demonstrated the correlation of enhanced Z_{DR} and K_{DP} near −15°C with dendritic growth and enhanced surface snowfall rates (Bechini et al. 2013; Andrić et al. 2013; Griffin et al. 2014; Schrom et al. 2015; Kennedy and Rutledge 2011). Meanwhile, below this isotherm level around 5.2 km, we see decreased Z_{DR} and K_{DP} and increased ρ_{HV} and Z_H, indicating a transition to the large aggregate formation and again consistent with literature and with the transition to dry snow (aggregate) typing seen in Fig. 12a.

Figure 14 shows a time slice from 0329 UTC 28 December 2021 (storm period 3) that represents a contrasting case to the time slice in Fig. 13. One obvious difference is that the echo top heights are much lower in Fig. 13, which is partly an indication of weaker storm intensity and is likely related to less overall IVT present in the region (Fig. 2). There is also a lack of an enhanced band of Z_{DR} and K_{DP} around the −15°C isotherm, with overall lower Z_{DR} and Z_H, indicating less intense precipitation, smaller crystals, likely formed primarily via diffusional growth, and lower overall snowfall accumulation during this period. Since Fig. 14 is relatively representative of storm periods 2–4, this dual-pol information supports the conclusions of enhanced aggregate formation in storm period 1 and a mix of crystals and weaker aggregate formation in all other periods as seen in the hydrometeor classification algorithm in Fig. 12. However, despite weaker overall intensity observed with the radar, the disdrometer (Fig. 4) observed very high counts of small crystals and relatively high precipitation rates during storm period 3. One possible explanation for this is blowing snow, although this would have had to occur at relatively low wind speeds since a wind speed filter was applied to disdrometer data. A second possible explanation is secondary ice production, as there is slightly negative Z_{DR} (which could indicate either vertical crystals or conical graupel, the latter of which would be convincing evidence) and Z_H co-located to the left of BCKa observed in Fig. 14 (Bringi et al. 2017). However, since the −5°C line and therefore the zone needed for the Hallett–Mossop process to take place is located very close to and in some cases below the surface in both Figs. 13 and 14 and there is no evidence of graupel production in the hydrometeor classification algorithm or elsewhere, no conclusive statement about secondary ice production can be made (Hallett and Mossop 1974).

In summary, the size of crystals and small dry aggregates observed in Fig. 14 is smaller as compared to the size of large dry and wet aggregate mix seen in Fig. 13. This is supported by hydrometeor typing from dual-pol variables (Fig. 12) and from the recorded disdrometer data. According to Ishizaka et al. (2016), the snowfall density for aggregates tends to be less than that of small crystals. This tendency toward lower-density snow can be further compounded once the snow is on the surface because pockets of air left between large aggregates reduce snowpack density. However, on 24 December, a near-surface freezing level caused a thin layer of wet snow in Fig. 12a; wet snow is partially melted ice; hence, it has higher water content and therefore density at the surface than dry aggregates (Bechini and Chandrasekar 2015).

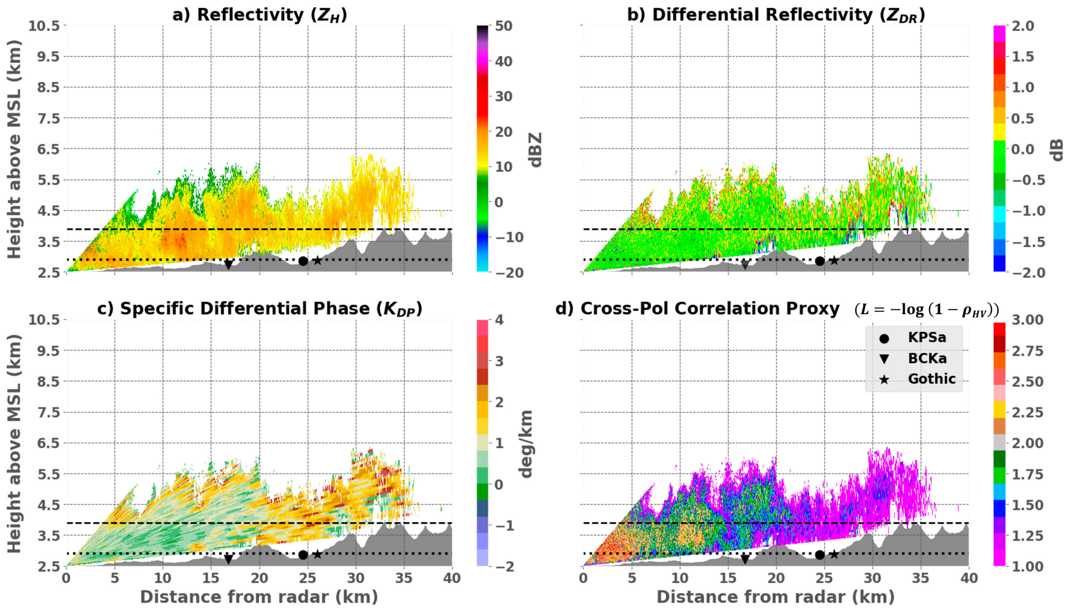

FIG. 14. As in Fig. 12, but at 0329:45 UTC 28 Dec 2021 (during storm period 3).

These precipitation types can also be related back to wind patterns and direction as well as to thermodynamic structures. For instance, areas of turbulence (Fig. 8) generally corresponded with regions of hydrometeors classified as aggregates, especially in Figs. 12b–d. These areas were on the windward side of the terrain, aligning with the theory that enhanced crystal growth was produced by weak generating cells induced by low-level shear (Geerts et al. 2015; Medina and Houze 2015; Houze and Medina 2005; Medina et al. 2005). The latter three storm periods appear to be more stratiform in nature than storm period 1, which had deeper radar echo tops and evidence of stronger generating cells that may have been the driving mechanism behind the consistent and large aggregates observed at the surface (Figs. 4 and 12). This is consistent with Houze and Medina (2005), who found that even where flow is stable, generating cells can be orographically generated; especially during this analysis period, there is no evidence that any of the convective features observed were instability driven. It is also possible, based on evidence of accelerating wind over the crest of terrain to the direct southwest of the East River Valley in Fig. 7b, that downslope flow was a mechanism for generating updrafts and turbulence in the region observed in storm period 1 (Pokharel et al. 2017; Geerts et al. 2015; Strauss et al. 2015). Geerts et al. (2015) suggest these two mechanisms may not be mutually exclusive. Evidence that there is a strong link between airflow over topography (Figs. 3 and 7), the generation of turbulence (Fig. 8), and the microphysical characteristics of hydrometeor generation that result in enhanced precipitation at the surface (Figs. 11–14). This can be seen quantitatively in the relationship between low-level turbulence, defined by spectral width in the lowest radar gate, and surface precipitation rates (Fig. 15). Figure 15 shows that at both sites, higher turbulence was weakly positively correlated with higher precipitation rates, and that precipitation rates above 2 mm h^{-1} did not seem to be observed until a certain spectral width threshold was passed at each site. This is evidence of turbulence as a mechanism for enhanced precipitation. Furthermore, based on evidence from Fig. 8 and total precipitation amounts, it seems probable that the dominant precipitation mechanism associated with turbulence generation preferentially occurred at BCK.

5. Conclusions

A significant multiday cold-season precipitation event in the East River watershed of the Upper Colorado River basin was examined in detail using in situ measurements, radiosonde measurements, and dual-pol X-band radar data from the SPLASH and SAIL field campaigns. This region is typically blocked from view of the Grand Junction WSR-88D radar, so this study provides novel insights into the microphysical characteristics during a snowfall event in the intermountain valley of the East River.

Between 23 December 2021 and 1 January 2022, four distinct precold frontal warm-sector precipitation periods were identified using integrated water vapor transport from reanalysis data and particle size and count from disdrometers at the surface: 0300 UTC 23 December–0000 UTC 25 December (storm period 1), 1200–2200 UTC 26 December (storm period 2), 0000–1200 UTC 28 December (storm period 3), and 0600 UTC 30 December–1600 UTC 31 December (storm period 4). The four periods were found to align with four distinct AR events, and storms experienced solely frozen precipitation types.

The results of this study show, consistent with results from previous literature, that empirical relationships of microphysical characteristics with known orographic precipitation processes can be applied to regions of highly complex terrain such as the ERW. Dual-pol variables were examined at two sites (KPS and BCK), and at both locations and across storm

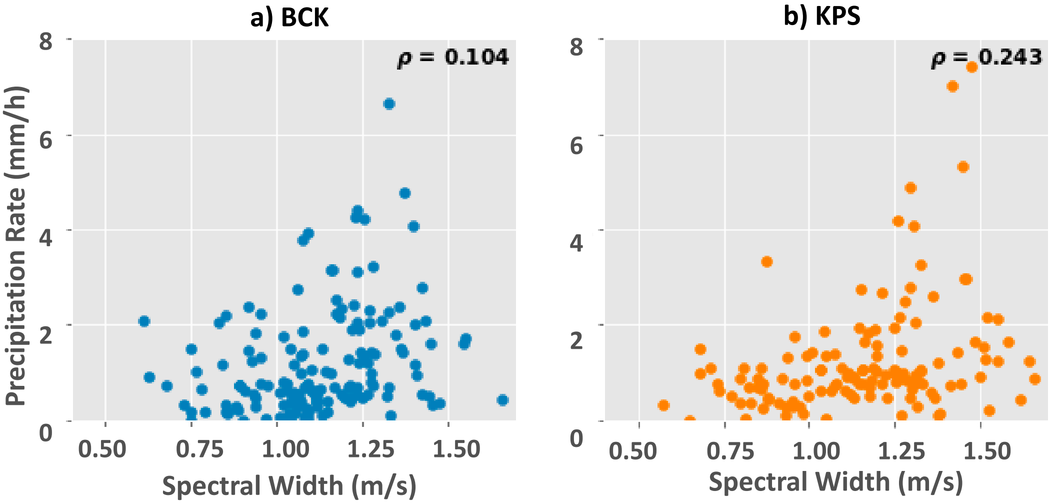

FIG. 15. Scatterplots of radar spectral width averaged over the radar gate closest to (a) BCK and (b) KPS vs the precipitation rate as recorded by the disdrometer, with the Spearman correlation coefficient displayed in the upper right-hand corner. Datasets were aggregated over time to the greatest common denominator of time interval to account for the temporal mismatch.

periods, depositional dendritic particle growth, as demonstrated by Z_{DR} and K_{DP} maximums coinciding with a ρ_{HV} minimum and a strong Z_H gradient, was observed at and above the −15°C isotherm (Fig. 11). Below the depositional dendritic growth zone, lower values of Z_{DR} and K_{DP} coincided with higher Z_H and ρ_{HV} indicating the formation of larger isotropic particles starting at around and just above the −5° isotherm (Fig. 11). High values of ρ_{HV} and near zero Z_{DR} values, coupled with disdrometer data showing a wide distribution of particle sizes, suggest that at across all time periods, at least a fraction of the dendritic particles were forming large, more isotropic particles. The measurement of enhanced K_{DP} and Z_{DR} with intense snowfall rates and dendritic particle growth at upper levels coupled with increased ρ_{HV} below the −15°C isotherm and observations of large isotropic particles at the surface during all storm periods is consistent with patterns observed in numerous studies of stratiform winter precipitation (e.g., Andrić et al. 2013; Kumjian et al. 2014; Schneebeli et al. 2013).

Larger isotropic particles could have formed via aggregation or riming processes. The analysis period exhibited very limited evidence of riming: large variations in Z_H at low levels were not observed, nor were significant periods of negative Z_{DR} or near-zero K_{DP}, and so it is unlikely riming processes occurred (Kneifel and Moisseev 2020). Riming processes also require warmer temperatures (Rogers and Yau 1989) than were observed during the analysis period (Fig. 3). In addition, although there was disdrometer evidence of significant counts of ice crystals reaching the surface during storm periods 2–4, with especially large concentrations during storm period 3 (Fig. 4), secondary ice production is plausible, but the lack of riming evidence in dual-polarization signatures prevents any conclusive statement from the data available.

In contrast, the analysis period exhibited significant evidence for aggregation processes, both in the observed polarimetric signatures and the likely turbulence mechanisms. For instance, the presence of dendrites aloft was established via dual-pol signatures, and this alone indicates aggregation is likely to occur. The observed decrease of Z_{DR} and K_{DP} below the −15°C isotherm is an indication of a reduction in particle bulk density occurring via aggregation. Furthermore, the temperature profiles during the time indicate temperature favorable to aggregate formation (from −15° to −5°C) in the lower atmosphere, and ρ_{HV} remains high throughout the lower levels of the atmosphere, indicating the presence of only one main mechanism of particle growth. Indeed, the hydrometeor algorithm confirmed the conclusions reached from these signatures and classified the larger particles as dry snow, i.e., aggregates (Fig. 12). The observed polarimetric signatures and conclusions about aggregate formation were also consistent with camera images at KPS and BCK (Fig. S6).

Areas of increased turbulence associated with aggregate particle growth were observed at various locations in the radar-observed along-valley azimuth and most often windward of terrain (Fig. 8). There are two possible mechanisms for the generation of turbulence: turbulence in the wake of downslope flow, as presented by Pokharel et al. (2017), and turbulence generated by a shear layer over a blocked flow pattern, as proposed by Houze and Medina (2005); the two mechanisms are not necessarily mutually exclusive. However, although downslope accelerations are possible and even likely in storm period 1, without additional multidirectional wind data, the presence of this mechanism cannot be confirmed. Meanwhile, the generation of a shear layer just above terrain height has been found to result from the decoupling of the synoptic cross-barrier flow and local terrain-dominated flow; this pattern was seen in wind and stability observations during this analysis. Given the high stability, boundary layer shear may have existed and could have plausibly been induced by local blocking although, given the lack of spatially coherent wind data, this cannot be stated conclusively.

Regardless of the mechanism, turbulence has been found to drive enhanced aggregation processes, and this was supported by dual-polarization signatures and disdrometer size and precipitation rate data over the storm period. Disdrometer data indicated particles had higher diameter maximums and drop size distribution ranges during storm period 1 as compared to the other three periods at KPS (Fig. 9). At BCK, storm period 1 and storm period 3 had comparably large ranges of particle diameters, but storm period 1 had these high values over a considerably longer window of time (Fig. 9). This indicates that the aggregation processes were weaker during storm periods 2–4 than in storm period 1; this could potentially be related to temporal differences in turbulence generation.

Under the conditions for turbulence generation by downslope wind in a stratiform precipitation regime, the rapid transition of dendrites into aggregates as they fall through the −15°C isotherm is the most likely mechanism for enhanced aggregate formation. In contrast, the production of aggregates from turbulence generation via shear in the boundary layer region is likely to take the form of the seeder–feeder effect. Generating cells have been identified as one source of the seeder–feeder process by Kumjian et al. (2014). Detection of these cells has been found to correspond with enhanced streamers of Z_H aloft; they are often found windward of orography and support orographic precipitation enhancement. Evidence of this pattern is observed throughout the event but most prominently in storm period 1, although it cannot be concluded whether this was driven by shear or convective instability (Fig. S5). As BCK is closer to the windward side of its nearby orography, generating cells created by the preferential turbulence in this region seen in Fig. 8 could be one explanation of higher precipitation amounts as compared to KPS, which is much further from its nearby orography. Evidence for aggregate production via enhanced turbulence across regions of shear can be seen in Figs. 6, 8, and 11; boundary layer shear was present and resulting enhanced turbulence corresponded with areas of enhanced particle growth via aggregation as observed by dual-pol signatures.

The radar-observed microphysical characteristics such as particle size, type, and structure also yield information about the density of the hydrometeors (Ishizaka et al. 2016). Since snow parameters are codependent, this can affect the density of fresh snowfall and in turn the snow-to-liquid ratio (SLR) of the resultant snowpack, which is calculated from the measured precipitation amount divided by snowfall depth (Ishizaka et al. 2016; Hurwitz et al. 2020; Alcott and Steenburgh 2010). For instance, turbulence-induced aggregation, in the absence of other processes, should lead to large, low-density snow and generally higher SLR values (i.e., above 10) at the surface (Alcott and Steenburgh 2010; Roebber et al. 2003). Large aggregates can also create air pockets when accumulating on the land surface, further lowering the density of snowpack, and generally increasing SLR (Ishizaka et al. 2016; Nguyen et al. 2019; Roebber et al. 2003). Thus, based on theory alone, we would expect SLRs to be above 10 for all periods and highest during storm period 1. Other factors impact SLR, however: at surface temperatures near freezing, melt can occur leading to lower SLRs (Alcott and Steenburgh 2010). Additionally, wind scouring and deposition decrease and increase SLRs, respectively, as they can both remove and deposit more snow in a location than originally fell. Analysis of the limited available SLR data from a nearby site that is higher in elevation and using a different time scale than data collected at KPS and BCK (Fig. S7; Bonner et al. 2022) does not align well with the patterns expected from the microphysics at the two sites. This suggests one or both environmental confounding factors (e.g., melt, blowing snow) are at play, possibly in addition to effects from spatial and temporal mismatch; in particular, during storm period 1 the temperature was near freezing, indicating surface melt was likely occurring. This makes it difficult to draw a clear relationship between hydrometeor density and surface SLR in this analysis.

This study is one example of how using X-band radar data, surface, and upper air datasets to understand microphysical growth processes can allow us to use phenomenological observations to develop insights into the fundamental relationships between the terrain, atmospheric dynamics, and atmospheric thermodynamics that govern precipitation processes and resulting snow density. Given the fact that the spatial scales of cloud microphysical interactions are orders of magnitude smaller than that of even the highest resolution atmospheric model, microphysical relationships must necessarily be parameterized in atmospheric models for the foreseeable future. Consequently, there is a need to better understand these relationships and reduce uncertainty in connections between atmospheric and surface snow parameters (Hurwitz et al. 2020). Ultimately, this allows for advancements in the accurate modeling of surface snowpack and a better understanding of hydrometeorology in this watershed.

Acknowledgments. The authors thank NOAA PSL for leading the SPLASH campaign and providing access to the SPLASH datasets. We would also like to thank Dr. W. Ryan Currier for his feedback and discussion of paper material, especially regarding snow accumulation, as well as Dr. Christopher Castro for advice on synoptic portrayals of this event. We would like to additionally thank Dr. Benjamin Moore for his technological expertise and data support on the analysis of atmospheric river events and synoptic-scale features, and billy barr of Rocky Mountain Biological Laboratory for his work in support of scientific data collection in the East River watershed. Heflin's contribution was supported in part by each of the following sources: the NOAA EPP/MSI Student Scholarship Program, NOAA PSL, and the Office of Science, U.S. Department of Energy, Office of Biological and Environmental Research as part of the Regional and Global Model Analysis program area. Feldman's contribution was supported by the U.S. Department of Energy, Office of Science, Office of Biological and Environmental Research, and the Atmospheric System Research under U.S. Department of Energy Contract DE-AC02-05CH11231. Venkatachalam, Biswas, and Kennedy are supported via Colorado State University by NOAA PSL and the DOE ARM Program. This research was also supported by NOAA Cooperative Agreements NA17OAR4320101 and NA22OAR4320151.

Data availability statement. The near-surface meteorological instrumentation at both field sites was collected as part of a radiation study by NOAA's Global Monitoring Laboratory and can be obtained from https://gml.noaa.gov/grad/splash.html. The SPLASH radar data will be made publicly available on the PSL web page shortly; until then, please e-mail the corresponding author for access. SPLASH disdrometer data are available at https://psl.noaa.gov/data/obs/datadisplay/. Data from the SAIL field campaign were obtained from an Atmospheric Radiation Measurement (ARM) User Facility, a U.S. Department of Energy (DOE) Office of Science user facility managed by the Biological and Environmental Research Program accessible at https://adc.arm.gov/discovery/#/results/site_code::guc. The ERA5-Land hourly dataset, including IVT and all variables used, can be obtained from Copernicus at https://doi.org/10.24381/cds.e2161bac.

REFERENCES

Abel, M. R., A. Hall, and R. G. Fovell, 2009: Blocking in areas of complex topography, and its influence on rainfall distribution. *J. Atmos. Sci.*, **66**, 508–518, https://doi.org/10.1175/2008JAS2689.1.

Aikins, J., K. Friedrich, B. Geerts, and B. Pokharel, 2016: Role of a cross-barrier jet and turbulence on winter orographic snowfall. *Mon. Wea. Rev.*, **144**, 3277–3300, https://doi.org/10.1175/MWR-D-16-0025.1.

Alcott, T. I., and W. J. Steenburgh, 2010: Snow-to-liquid ratio variability and prediction at a high-elevation site in Utah's Wasatch Mountains. *Wea. Forecasting*, **25**, 323–337, https://doi.org/10.1175/2009WAF2222311.1.

Allabakash, S., S. Lim, V. Chandrasekar, K. H. Min, J. Choi, and B. Jang, 2019: X-band dual-polarization radar observations of snow growth processes of a severe winter storm: Case of 12 December 2013 in South Korea. *J. Atmos. Oceanic Technol.*, **36**, 1217–1235, https://doi.org/10.1175/JTECH-D-18-0076.1.

Andrić, J., M. R. Kumjian, D. S. Zrnić, J. M. Straka, and V. M. Melnikov, 2013: Polarimetric signatures above the melting layer in winter storms: An observational and modeling study. *J. Appl. Meteor. Climatol.*, **52**, 682–700, https://doi.org/10.1175/JAMC-D-12-028.1.

ARM, 2021a: X-Band Precipitation Radar (XPRECIPRADAR). ARM Mobile Facility (GUC); Supplemental Facility 2 (S2), Accessed 15 June 2023, https://www.arm.gov/capabilities/instruments/xprecipradar.

——, 2021b: Gridded Sonde VAP Product (GRIDDEDSONDE). ARM Mobile Facility (GUC) Gunnison, CO; AMF2 (main site for SAIL) (M1), accessed 15 June 2023, http://dx.doi.org/10.5439/1350631.

Armijo, L., 1969: A Theory for the determination of wind and precipitation velocities with Doppler radars. *J. Atmos. Sci.*, **26**, 570–573, https://doi.org/10.1175/1520-0469(1969)026<0570:ATFTDO>2.0.CO;2.

Bailey, M. P., and J. Hallett, 2009: A comprehensive habit diagram for atmospheric ice crystals: Confirmation from the laboratory, AIRS II, and other field studies. *J. Atmos. Sci.*, **66**, 2888–2899, https://doi.org/10.1175/2009JAS2883.1.

Bechini, R., and V. Chandrasekar, 2015: A semisupervised robust hydrometeor classification method for dual-polarization radar applications. *J. Atmos. Oceanic Technol.*, **32**, 22–47, https://doi.org/10.1175/JTECH-D-14-00097.1.

——, L. Baldini, and V. Chandrasekar, 2013: Polarimetric radar observations in the ice region of precipitating clouds at C-band and X-band radar frequencies. *J. Appl. Meteor. Climatol.*, **52**, 1147–1169, https://doi.org/10.1175/JAMC-D-12-055.1.

Bharadwaj, N., V. Chandrasekar, and F. Junyent, 2010: Signal processing system for the CASA integrated project I radars. *J. Atmos. Oceanic Technol.*, **27**, 1440–1460, https://doi.org/10.1175/2010JTECHA1415.1.

Bonner, H. M., E. Smyth, M. S. Raleigh, and E. E. Small, 2022: A meteorology and snow data set from adjacent forested and meadow sites at Crested Butte, CO, USA. *Water Resour. Res.*, **58**, e2022WR033006, https://doi.org/10.1029/2022WR033006.

Brandes, E. A., K. Ikeda, G. Zhang, M. Schönhuber, and R. M. Rasmussen, 2007: A statistical and physical description of hydrometeor distributions in Colorado snowstorms using a video disdrometer. *J. Appl. Meteor. Climatol.*, **46**, 634–650, https://doi.org/10.1175/JAM2489.1.

Bringi, V. N., and V. Chandrasekar, 2001: *Polarimetric Doppler Weather Radar: Principles and Applications*. Cambridge University Press, 636 pp.

——, P. C. Kennedy, G.-J. Huang, C. Kleinkort, M. Thurai, and B. M. Notaroš, 2017: Dual-polarized radar and surface observations of a winter graupel shower with negative Z_{dr} column. *J. Appl. Meteor. Climatol.*, **56**, 455–470, https://doi.org/10.1175/JAMC-D-16-0197.1.

Bureau of Reclamation, 2024: Near-term Colorado River operation: Final supplemental environmental impact statement. U.S. Department of the Interior Regions 7 and 8, 1 pp.

Bytheway, J. L., W. R. Currier, M. R. Abel, K. Mahoney, and R. Cifelli, 2024: Evaluation of wintertime precipitation estimates and forecasts in the mountains of Colorado. *J. Hydrometeor.*, **25**, 565–579, https://doi.org/10.1175/JHM-D-23-0158.1.

Campbell, L. S., and W. J. Steenburgh, 2014: Finescale orographic precipitation variability and gap-filling radar potential in Little Cottonwood Canyon, Utah. *Wea. Forecasting*, **29**, 912–935, https://doi.org/10.1175/WAF-D-13-00129.1.

Capozzi, V., C. Annella, M. Montopoli, E. Adirosi, G. Fusco, and G. Budillon, 2021: Influence of wind-induced effects on laser disdrometer measurements: Analysis and compensation strategies. *Remote Sens.*, **13**, 3028, https://doi.org/10.3390/rs13153028.

Chandrasekar, V., R. Keränen, S. Lim, and D. Moisseev, 2013: Recent advances in classification of observations from dual polarization weather radars. *Atmos. Res.*, **119**, 97–111, https://doi.org/10.1016/j.atmosres.2011.08.014.

——, R. M. Beauchamp, and R. Bechini, 2023: Data quality, data science, and engineering of weather radars. *Introduction to Dual Polarization Weather Radar: Fundamentals, Applications, and Networks*, 1st ed. Cambridge University Press, 294–344.

CoCoRAHS, 2021: Crested Butte 6.2 N daily precipitation report (CO-GN-18) 12/24/21. Community Collaborative Rain, Hail, and Snow Network, accessed 28 June 2023.

de Boer, G., and Coauthors, 2023: Supporting advancement in weather and water prediction in the Upper Colorado River Basin: The SPLASH campaign. *Bull. Amer. Meteor. Soc.*, **104**, E1853–E1874, https://doi.org/10.1175/BAMS-D-22-0147.1.

DeVoir, G., 2002: A quick review of snow microphysics and its relation to heavy snow forecasting. *NWS CTP Winter Weather Workshop*, State College, PA, NWS, 3–15, https://www.slideserve.com/jaron/a-quick-review-of-snow-microphysics-and-its-relation-to-heavy-snow-forecasting.

Dolan, B., and S. A. Rutledge, 2009: A theory-based hydrometeor identification algorithm for X-band polarimetric radars. *J.*

Atmos. Oceanic Technol., **26**, 2071–2088, https://doi.org/10.1175/2009JTECHA1208.1.

Douglas, R. H., K. L. S. Gunn, and J. S. Marshall, 1957: Pattern in the vertical of snow generation. *J. Atmos. Sci.*, **14**, 95–114, https://doi.org/10.1175/1520-0469(1957)014<0095:PITVOS>2.0.CO;2.

Doviak, R. J., and D. S. Zrnić, 1993: Doppler spectra of weather signals. *Doppler Radar and Weather Observations*, Academic Press, 87–121.

Dzambo, A. M., and D. D. Turner, 2016: Characterizing relative humidity with respect to ice in midlatitude cirrus clouds as a function of atmospheric state. *J. Geophys. Res. Atmos.*, **121**, 12 253–12 269, https://doi.org/10.1002/2015JD024643.

Eidhammer, T., H. Morrison, D. Mitchell, A. Gettelman, and E. Erfani, 2017: Improvements in global climate model microphysics using a consistent representation of ice particle properties. *J. Climate*, **30**, 609–629, https://doi.org/10.1175/JCLI-D-16-0050.1.

Feldman, D., and Coauthors, 2021: Surface Atmosphere Integrated Field Laboratory (SAIL) Science Plan. Rep. DOE/SC-ARM-21-004, 83 pp., https://www.arm.gov/publications/programdocs/doe-sc-arm-21-004.pdf.

Feldman, D. R., and Coauthors, 2023: The Surface Atmosphere Integrated Field Laboratory (SAIL) Campaign. *Bull. Amer. Meteor. Soc.*, **104**, E2192–E2222, https://doi.org/10.1175/BAMS-D-22-0049.1.

Frasier, S. J., F. Kabeche, J. Figueras i Ventura, H. Al-Sakka, P. Tabary, J. Beck, and O. Bousquet, 2013: In-place estimation of wet radome attenuation at X band. *J. Atmos. Oceanic Technol.*, **30**, 917–928, https://doi.org/10.1175/JTECH-D-12-00148.1.

Geerts, B., Q. Miao, and Y. Yang, 2011: Boundary layer turbulence and orographic precipitation growth in cold clouds: Evidence from profiling airborne radar data. *J. Atmos. Sci.*, **68**, 2344–2365, https://doi.org/10.1175/JAS-D-10-05009.1.

——, Y. Yang, R. Rasmussen, S. Haimov, and B. Pokharel, 2015: Snow growth and transport patterns in orographic storms as estimated from airborne vertical-plane dual-Doppler radar data. *Mon. Wea. Rev.*, **143**, 644–665, https://doi.org/10.1175/MWR-D-14-00199.1.

Goff, J. A., and S. Gratch, 1945: Thermodynamic properties of moist air. *Amer. Soc. Heat. Vent. Eng. Trans.*, **51**, 125–157.

Gonzalez, S., J. Bech, M. Udina, B. Codina, A. Paci, and L. Trapero, 2019: Decoupling between precipitation processes and mountain wave induced circulations observed with a vertically pointing K-band Doppler radar. *Remote Sens.*, **11**, 1034, https://doi.org/10.3390/rs11091034.

González, S., J. Bech, A. Garcia-Benadí, M. Udina, B. Codina, L. Trapero, A. Paci, and J.-F. Georgis, 2021: Vertical structure and microphysical observations of winter precipitation in an inner valley during the Cerdanya-2017 field campaign. *Atmos. Res.*, **264**, 105826, https://doi.org/10.1016/j.atmosres.2021.105826.

Griffin, E. M., T. J. Schuur, A. V. Ryzhkov, H. D. Reeves, and J. C. Picca, 2014: A polarimetric and microphysical investigation of the Northeast blizzard of 8–9 February 2013. *Wea. Forecasting*, **29**, 1271–1294, https://doi.org/10.1175/WAF-D-14-00056.1.

Guan, B., and D. E. Waliser, 2019: Tracking atmospheric rivers globally: Spatial distributions and temporal evolution of life cycle characteristics. *J. Geophys. Res. Atmos.*, **124**, 12 523–12 552, https://doi.org/10.1029/2019JD031205.

Hallett, J., and S. C. Mossop, 1974: Production of secondary ice particles during the riming process. *Nature*, **249**, 26–28, https://doi.org/10.1038/249026a0.

Helmus, J. J., and S. M. Collis, 2016: The Python ARM Radar Toolkit (Py-ART), a library for working with weather radar data in the Python Programming Language. *J. Open Res. Software*, **4**, 25, https://doi.org/10.5334/jors.119.

Hersbach, H., and Coauthors, 2020: The ERA5 global reanalysis. *Quart. J. Roy. Meteor. Soc.*, **146**, 1999–2049, https://doi.org/10.1002/qj.3803.

Heymsfield, G. M., 1979: Doppler radar study of a warm frontal region. *J. Atmos. Sci.*, **36**, 2093–2107, https://doi.org/10.1175/1520-0469(1979)036<2093:DRSOAW>2.0.CO;2.

Houze, R. A., Jr., 2012: Orographic effects on precipitating clouds. *Rev. Geophys.*, **50**, RG1001, https://doi.org/10.1029/2011RG000365.

——, and S. Medina, 2005: Turbulence as a mechanism for orographic precipitation enhancement. *J. Atmos. Sci.*, **62**, 3599–3623, https://doi.org/10.1175/JAS3555.1.

——, J. D. Locatelli, and P. V. Hobbs, 1976: Dynamics and cloud microphysies of the rainbands in an occluded frontal system. *J. Atmos. Sci.*, **33**, 1921–1936, https://doi.org/10.1175/1520-0469(1976)033<1921:DACMOT>2.0.CO;2.

Hurwitz, M. M., and Coauthors, 2020: Six priorities for investment in snow research and product development. *Bull. Amer. Meteor. Soc.*, **101**, E2025–E2029, https://doi.org/10.1175/BAMS-D-20-0218.1.

Ikeda, K., and Coauthors, 2010: Simulation of seasonal snowfall over Colorado. *Atmos. Res.*, **97**, 462–477, https://doi.org/10.1016/j.atmosres.2010.04.010.

——, and Coauthors, 2021: Snowfall and snowpack in the Western U.S. as captured by convection permitting climate simulations: Current climate and pseudo global warming future climate. *Climate Dyn.*, **57**, 2191–2215, https://doi.org/10.1007/s00382-021-05805-w.

Ishizaka, M., H. Motoyoshi, S. Yamaguchi, S. Nakai, T. Shiina, and K. Muramoto, 2016: Relationships between snowfall density and solid hydrometeors, based on measured size and fall speed, for snowpack modeling applications. *Cryosphere*, **10**, 2831–2845, https://doi.org/10.5194/tc-10-2831-2016.

James, T., A. Evans, E. Madly, and K. Kelly, 2014: The economic importance of the Colorado River to the basin region. L William Seidman Research Institute Final Rep., 54 pp., https://businessforwater.org/wp-content/uploads/2016/12/PTF-Final-121814.pdf.

Judson, A., and N. Doesken, 2000: Density of freshly fallen snow in the central Rocky Mountains. *Bull. Amer. Meteor. Soc.*, **81**, 1577–1588, https://doi.org/10.1175/1520-0477(2000)081<1577:DOFFSI>2.3.CO;2.

Keeler, J. M., R. M. Rauber, B. F. Jewett, G. M. McFarquhar, R. M. Rasmussen, L. Xue, C. Liu, and G. Thompson, 2017: Dynamics of cloud-top generating cells in winter cyclones. Part III: Shear and convective organization. *J. Atmos. Sci.*, **74**, 2879–2897, https://doi.org/10.1175/JAS-D-16-0314.1.

Kennedy, P. C., and S. A. Rutledge, 2011: S-band dual-polarization radar observations of winter storms. *J. Appl. Meteor. Climatol.*, **50**, 844–858, https://doi.org/10.1175/2010JAMC2558.1.

King, M. D., and Coauthors, 2003: Cloud and aerosol properties, precipitable water, and profiles of temperature and water vapor from MODIS. *IEEE Trans. Geosci. Remote Sens.*, **41**, 442–458, https://doi.org/10.1109/TGRS.2002.808226.

Kingsmill, D. E., P. J. Neiman, B. J. Moore, M. R. Abel, S. E. Yuter, and F. M. Ralph, 2013: Kinematic and thermodynamic structures of Sierra Barrier jets and overrunning atmospheric rivers during a landfalling winter storm in Northern California. *Mon. Wea. Rev.*, **141**, 2015–2036, https://doi.org/10.1175/MWR-D-12-00277.1.

Kneifel, S., and D. Moisseev, 2020: Long-term statistics of riming in nonconvective clouds derived from ground-based Doppler cloud radar observations. *J. Atmos. Sci.*, **77**, 3495–3508, https://doi.org/10.1175/JAS-D-20-0007.1.

Kropfli, R. A., and N. M. Kohn, 1978: Persistent horizontal rolls in the urban mixed layer as revealed by dual-Doppler radar. *J. Appl. Meteor.*, **17**, 669–676, https://doi.org/10.1175/1520-0450(1978)017<0669:PHRITU>2.0.CO;2.

Kumjian, M. R., 2013a: Principles and applications of dual-polarization weather radar. Part I: Description of the polarimetric radar variables. *J. Oper. Meteor.*, **1**, 226–242, https://doi.org/10.15191/nwajom.2013.0119.

——, 2013b: Principles and applications of dual-polarization weather radar. Part II: Warm- and cold-season applications. *J. Oper. Meteor.*, **1**, 243–264, https://doi.org/10.15191/nwajom.2013.0120.

——, S. A. Rutledge, R. M. Rasmussen, P. C. Kennedy, and M. Dixon, 2014: High-resolution polarimetric radar observations of snow-generating cells. *J. Appl. Meteor. Climatol.*, **53**, 1636–1658, https://doi.org/10.1175/JAMC-D-13-0312.1.

Lim, S., R. Cifelli, V. Chandrasekar, and S. Y. Matrosov, 2013a: Precipitation classification and quantification using X-band dual-polarization weather radar: Application in the hydrometeorology testbed. *J. Atmos. Oceanic Technol.*, **30**, 2108–2120, https://doi.org/10.1175/JTECH-D-12-00123.1.

——, D. Moisseev, V. Chandrasekar, and D.-R. Lee, 2013b: Classification and quantification of snow based on spatial variability of radar reflectivity. *J. Meteor. Soc. Japan*, **91**, 763–774, https://doi.org/10.2151/jmsj.2013-603.

Liu, C., and Coauthors, 2017: Continental-scale convection-permitting modeling of the current and future climate of North America. *Climate Dyn.*, **49**, 71–95, https://doi.org/10.1007/s00382-016-3327-9.

Liu, H., and V. Chandrasekar, 2000: Classification of hydrometeors based on polarimetric radar measurements: Development of fuzzy logic and neuro-fuzzy systems, and in situ verification. *J. Atmos. Oceanic Technol.*, **17**, 140–164, https://doi.org/10.1175/1520-0426(2000)017<0140:COHBOP>2.0.CO;2.

Lukas, J., and B. Harding, 2020: Current understanding of Colorado River basin climate and hydrology. *Colorado River Basin Climate and Hydrology: State of the Science*, Western Water Assessment, University of Colorado Boulder, 42–81.

——, and E. Payton, 2020: Introduction. *Colorado River Basin Climate and Hydrology: State of the Science*, Western Water Assessment, University of Colorado Boulder, 31–41.

Lundquist, J., M. R. Abel, E. Gutmann, and S. Kapnick, 2019: Our skill in modeling mountain rain and snow is bypassing the skill of our observational networks. *Bull. Amer. Meteor. Soc.*, **100**, 2473–2490, https://doi.org/10.1175/BAMS-D-19-0001.1.

Maddox, R. A., J. Zhang, J. J. Gourley, and K. W. Howard, 2002: Weather radar coverage over the contiguous United States. *Wea. Forecasting*, **17**, 927–934, https://doi.org/10.1175/1520-0434(2002)017<0927:WRCOTC>2.0.CO;2.

Mancini, A., J. L. Salazar, R. M. Lebrón, and B. L. Cheong, 2018: A novel instrument for real-time measurement of attenuation of weather radar radome including its outer surface. Part I: The concept. *J. Atmos. Oceanic Technol.*, **35**, 953–973, https://doi.org/10.1175/JTECH-D-17-0083.1.

Marwitz, J. D., 1987: Deep orographic storms over the Sierra Nevada. Part I: Thermodynamic and kinematic structure. *J. Atmos. Sci.*, **44**, 159–173, https://doi.org/10.1175/1520-0469(1987)044<0159:DOSOTS>2.0.CO;2.

Medina, S., and R. A. Houze Jr., 2015: Small-scale precipitation elements in midlatitude cyclones crossing the California Sierra Nevada. *Mon. Wea. Rev.*, **143**, 2842–2870, https://doi.org/10.1175/MWR-D-14-00124.1.

——, B. F. Smull, R. A. Houze Jr., and M. Steiner, 2005: Cross-barrier flow during orographic precipitation events: Results from MAP and IMPROVE. *J. Atmos. Sci.*, **62**, 3580–3598, https://doi.org/10.1175/JAS3554.1.

Miller, J., 1998: CEDRIC: Custom editing and display of reduced information in Cartesian space. Tech. Rep., 130 pp., https://github.com/ai2es/hradar2updraft/blob/main/aux_docs/cedric.2009sep_doc.pdf.

Minder, J. R., D. R. Durran, and G. H. Roe, 2011: Mesoscale controls on the mountainside snow line. *J. Atmos. Sci.*, **68**, 2107–2127, https://doi.org/10.1175/JAS-D-10-05006.1.

Mott, R., V. Vionnet, and T. Grünewald, 2018: The seasonal snow cover dynamics: Review on wind-driven coupling processes. *Front. Earth Sci.*, **6**, 197, https://doi.org/10.3389/feart.2018.00197.

National Water and Climate Center, 2022: Butte SNOTEL site number 380. USDA Air and Water Database Public Reports, accessed 24 June 2023, https://wcc.sc.egov.usda.gov/nwcc/site?sitenum=380.

Neiman, P. J., M. R. Abel, B. J. Moore, F. M. Ralph, and E. M. Sukovich, 2013: Sierra Barrier jets, atmospheric rivers, and precipitation characteristics in Northern California: A composite perspective based on a network of wind profilers. *Mon. Wea. Rev.*, **141**, 4211–4233, https://doi.org/10.1175/MWR-D-13-00112.1.

Nguyen, C. M., M. Wolde, and A. Korolev, 2019: Determination of ice water content (IWC) in tropical convective clouds from X-band dual-polarization airborne radar. *Atmos. Meas. Tech.*, **12**, 5897–5911, https://doi.org/10.5194/amt-12-5897-2019.

NOAA JetStream, 2023: Radar images: Velocity. NOAA, accessed 30 June 2023, https://www.noaa.gov/jetstream/velocity.

NOAA Virtual Lab, 2022: Dual-pol precipitation flipchart – Forecaster references. NOAA Office of the Chief Learning Officer, accessed 20 June 2023, https://vlab.noaa.gov/web/oclo/dualpol.

OTT Hydromet, 2019: Technical data – OTT Parsivel Laser Weather Sensor. Accessed 15 June 2023, https://www.otthydromet.com/.

——, 2024: Operating instructions present weather sensor OTT Parsivel. OTT Instruction Manual, 52 pp., https://www.ott.com/download/operating-instructions-present-weather-sensor-ott-parsivel2-without-screen-heating-1/.

Oue, M., M. Galletti, J. Verlinde, A. Ryzhkov, and Y. Lu, 2016: Use of X-band differential reflectivity measurements to study shallow Arctic mixed-phase clouds. *J. Appl. Meteor. Climatol.*, **55**, 403–424, https://doi.org/10.1175/JAMC-D-15-0168.1.

Platnick, S., and Coauthors, 2017: MODIS Atmosphere L2 Cloud Product (06_L2). NASA MODIS Adaptive Processing System, Goddard Space Flight Center, accessed 7 January 2024, https://doi.org/10.5067/MODIS/MYD06_L2.061.

Pokharel, B., B. Geerts, X. Chu, and P. Bergmaier, 2017: Profiling radar observations and numerical simulations of a downslope wind storm and rotor on the lee of the Medicine Bow

Mountains in Wyoming. *Atmosphere*, **8**, 39, https://doi.org/10.3390/atmos8020039.

Ramelli, F., and Coauthors, 2021: Microphysical investigation of the seeder and feeder region of an Alpine mixed-phase cloud. *Atmos. Chem. Phys.*, **21**, 6681–6706, https://doi.org/10.5194/acp-21-6681-2021.

Rasmussen, R., and Coauthors, 2011: High-resolution coupled climate runoff simulations of seasonal snowfall over Colorado: A process study of current and warmer climate. *J. Climate*, **24**, 3015–3048, https://doi.org/10.1175/2010JCLI3985.1.

Rasmussen, R. M., and Coauthors, 2023: CONUS404: The NCAR–USGS 4-km long-term regional hydroclimate reanalysis over the CONUS. *Bull. Amer. Meteor. Soc.*, **104**, E1382–E1408, https://doi.org/10.1175/BAMS-D-21-0326.1.

Rea, D., R. M. Rauber, H. Hu, S. A. Tessendorf, S. W. Nesbitt, B. F. Jewett, and T. J. Zaremba, 2023: The contribution of subtropical moisture within an atmospheric river on moisture flux, cloud structure, and precipitation over the Salmon River Mountains of Idaho using moisture tracers. *J. Geophys. Res. Atmos.*, **128**, e2022JD037727, https://doi.org/10.1029/2022JD037727.

Roe, G. H., 2005: Orographic precipitation. *Annu. Rev. Earth Planet. Sci.*, **33**, 645–671, https://doi.org/10.1146/annurev.earth.33.092203.122541.

Roebber, P. J., S. L. Bruening, D. M. Schultz, and J. V. Cortinas Jr., 2003: Improving snowfall forecasting by diagnosing snow density. *Wea. Forecasting*, **18**, 264–287, https://doi.org/10.1175/1520-0434(2003)018<0264:ISFBDS>2.0.CO;2.

Rogers, R. R., and M. K. Yau, 1989: *A Short Course in Cloud Physics*. 3rd ed. Butterworth Heinemann, 290 pp.

Rudisill, W. J., A. N. Flores, H. P. Marshall, E. Siirila-Woodburn, D. R. Feldman, A. M. Rhoades, Z. Xu, and A. Morales, 2024: Cold-season precipitation sensitivity to microphysical parameterizations: Hydrologic evaluations leveraging snow lidar datasets. *J. Hydrometeor.*, **25**, 143–160, https://doi.org/10.1175/JHM-D-22-0217.1.

Rutz, J. J., and W. J. Steenburgh, 2012: Quantifying the role of atmospheric rivers in the interior western United States. *Atmos. Sci. Lett.*, **13**, 257–261, https://doi.org/10.1002/asl.392.

——, ——, and F. M. Ralph, 2014: Climatological characteristics of atmospheric rivers and their inland penetration over the western United States. *Mon. Wea. Rev.*, **142**, 905–921, https://doi.org/10.1175/MWR-D-13-00168.1.

——, ——, and ——, 2015: The inland penetration of atmospheric rivers over western North America: A Lagrangian analysis. *Mon. Wea. Rev.*, **143**, 1924–1944, https://doi.org/10.1175/MWR-D-14-00288.1.

Schneebeli, M., N. Dawes, M. Lehning, and A. Berne, 2013: High-resolution vertical profiles of X-band polarimetric radar observables during snowfall in the Swiss Alps. *J. Appl. Meteor. Climatol.*, **52**, 378–394, https://doi.org/10.1175/JAMC-D-12-015.1.

Schrom, R. S., M. R. Kumjian, and Y. Lu, 2015: Polarimetric radar signatures of dendritic growth zones within Colorado winter storms. *J. Appl. Meteor. Climatol.*, **54**, 2365–2388, https://doi.org/10.1175/JAMC-D-15-0004.1.

Shen, Y., Y. Chen, Y. Bi, D. Lyu, H. Chen, and S. Duan, 2022: Snowfall microphysics characterized by PARSIVEL disdrometer observations in Beijing from 2020 to 2022. *Remote Sens.*, **14**, 6025, https://doi.org/10.3390/rs14236025.

Sherwood, S. C., J. R. Lanzante, and C. L. Meyer, 2005: Radiosonde daytime biases and late-20th century warming. *Science*, **309**, 1556–1559, https://doi.org/10.1126/science.1115640.

Smith, R. B., 1979: The influence of mountains on the atmosphere. *Advances in Geophysics*, B. Saltzman, Ed., Vol. 21, Academic Press, 87–230, https://doi.org/10.1016/S0065-2687(08)60262-9.

Strauss, L., S. Serafin, S. Haimov, and V. Grubišić, 2015: Turbulence in breaking mountain waves and atmospheric rotors estimated from airborne *in situ* and Doppler radar measurements. *Quart. J. Roy. Meteor. Soc.*, **141**, 3207–3225, https://doi.org/10.1002/qj.2604.

Tessendorf, S. A., and Coauthors, 2019: A transformational approach to winter orographic weather modification research: The SNOWIE project. *Bull. Amer. Meteor. Soc.*, **100**, 71–92, https://doi.org/10.1175/BAMS-D-17-0152.1.

Tiira, J., D. N. Moisseev, A. von Lerber, D. Ori, A. Tokay, L. F. Bliven, and W. Petersen, 2016: Ensemble mean density and its connection to other microphysical properties of falling snow as observed in Southern Finland. *Atmos. Meas. Tech.*, **9**, 4825–4841, https://doi.org/10.5194/amt-9-4825-2016.

Troyan, D., 2013: Interpolated sounding value-added product. Rep. DOE/SC-ARM/TR-124, 18 pp., https://www.arm.gov/publications/tech_reports/doe-sc-arm-tr-124.pdf?id=96.

Vulpiani, G., M. Montopoli, L. D. Passeri, A. G. Gioia, P. Giordano, and F. S. Marzano, 2012: On the use of dual-polarized C-band radar for operational rainfall retrieval in mountainous areas. *J. Appl. Meteor. Climatol.*, **51**, 405–425, https://doi.org/10.1175/JAMC-D-10-05024.1.

Wasserstein, M. L., and W. J. Steenburgh, 2024: Diverse characteristics of extreme orographic snowfall events in Little Cottonwood Canyon, Utah. *Mon. Wea. Rev.*, **15**, 945–966, https://doi.org/10.1175/MWR-D-23-0206.1.

Xu, Z., E. R. Siirila-Woodburn, A. M. Rhoades, and D. Feldman, 2023: Sensitivities of subgrid-scale physics schemes, meteorological forcing, and topographic radiation in atmosphere-through-bedrock integrated process models: A case study in the Upper Colorado River basin. *Hydrol. Earth Syst. Sci.*, **27**, 1771–1789, https://doi.org/10.5194/hess-27-1771-2023.

Yin, M., and C. Yuan, 2022: Exploring the environmental conditions of snow particles using spaceborne triple-frequency radar measurements over ocean. *Remote Sens.*, **14**, 5512, https://doi.org/10.3390/rs14215512.

Zagrodnik, J. P., L. A. McMurdie, R. A. Houze Jr., and S. Tanelli, 2019: Vertical structure and microphysical characteristics of frontal systems passing over a three-dimensional coastal mountain range. *J. Atmos. Sci.*, **76**, 1521–1546, https://doi.org/10.1175/JAS-D-18-0279.1.